EUROPEAN FUSION DEVELOPMENT AGREEMENT

EFDA–JET–PR(04)71

W. Fundamenski, R.A. Pitts, G.F. Matthews, V. Riccardo, S. Sipilä
and EFDA JET contributors

ELM-averaged Power Exhaust on JET

ELM-averaged Power Exhaust on JET

W. Fundamenski[1], R.A. Pitts[2], G.F. Matthews[1], V. Riccardo[1], S. Sipilä[3]
and EFDA JET contributors*

[1]Euratom/UKAEA Fusion Association, Culham Science Centre, Abingdon, OX14 3DB, UK
[2]CRPP, Assoc. Euratom-EPFL, CH-1015, Lausanne, Switzerland
[3]Helsinki U. of Technology, Tekes-Euratom Assoc., PO Box 2200, FIN-02015 HUT, Finland
**See appendix of J. Pamela et al., "Overview of JET results", in Proc of 19th IAEA Fusion Energy Conference, Lyon, 2002 (IAEA, Vienna, 2003)*

Preprint of Paper to be submitted for publication in
Nuclear Fusion

ABSTRACT

The article describes experiments performed on JET over the past two years dedicated to characterising ELM-averaged power exhaust (based on time-averaged divertor power deposition profiles), with an emphasis on unfuelled, Type-I ELMy H-mode. Radial energy transport in the SOL is found to behave differently in the ion and electron channels: the former is dominated by (neo-)classical ion conduction, i.e. by diffusion of heat due to ion-ion collisions, while the later appears to be governed by turbulent convection, most likely driven by MHD interchange and/or drift-Alfven instabilities. Comparison of forward and reversed field experiments indicates that classical drifts can explain the observed in-out poloidal asymmetry in the heat loads deposited on the divertor. Whereas the role of ELMs needs further characterisation, a coherent picture of ELM-averaged power exhaust can be formed by considering the role of collisional heat diffusion in the highly dissipative SOL turbulence.

1. INTRODUCTION

1.1 MOTIVATION

Power exhaust is to fusion energy what landing is to aviation and what re-entry is to space travel. It may be less exciting than ignition (or blast-off), but it is no less important for the repeated operation of the device. In existing tokamaks, power exhaust is only a minor concern for the lifetime of first wall components, but it will be a critical issue in ITER. In more mundane terms, the exhaust of power from the core plasma via the scrape-off layer (SOL) and the associated energy fluxes on divertor plates and main chamber limiters, impose severe restrictions on the design of first wall components in ITER [Federici01]. Characterisation of power deposition profiles and improved understanding of SOL energy transport mechanisms are thus high priority tasks for the ITER project. Indeed, the absence of a credible theory for the radial heat diffusivity $\chi_{\perp}$, especially its functional dependence on local field and plasma variables, was considered in the ITER Physics Basis [ITER99] to be the weakest link in the predictive chain, preventing a true coupling of code and theory and reducing ITER extrapolation to empirical scalings of the power width, λ_q. This has motivated a series of JET experiments over the past two years dedicated to the study of power exhaust. Although these experiments are a natural extension of the work presented at the previous IAEA conference [Matthews03], they represent significant progress in the understanding of power exhaust on JET. The aim of the present article is thus threefold: 1) to review the previous JET experiments and the accompanying modelling activity in the light of more recent findings, 2) to present new experimental and interpretative work, situating it firmly in the context of previously published results, and 3) to form a coherent, up-to-date picture of ELM-averaged power exhaust, consistent with all available JET data. To achieve these goals, the article necessarily consists of a combination of original and previously published material. An attempt has been made to distinguish between the two as much as possible, eg. by indicating if a figure has previously appeared in the literature. Nonetheless the new contributions are generally mixed with previously published material. Original contributions

include the detailed analysis of reversed field experiments in Section 3, theory-experiment comparison of electron profile data in Section 4, and the systematic analysis of SOL turbulence in Section 5.

Whilst an analysis of ELM (transient) power exhaust is highly desirable, the divertor diagnostics have insufficient resolution to properly decouple the inter-ELM and ELM components of the deposited heat load. The present article is thus restricted to a discussion of ELM-averaged (steady-state) power exhaust; the term ELM-averaged denotes a temporal average over the steady-state (flat-top) phase of an ELMy H-mode discharge. The article is organised as follows: Section 1 introduces the general concepts of power exhaust and gives a brief overview of JET power exhaust diagnostics. Section 2 is devoted to an improved interpretation of forward field experiments, which although previously presented, have benefited from more recent results. Section 3 discusses the most notable of these, namely the reversed field experiments recently performed on JET [Pitts05]. Section 4 reviews the transport of electron thermal energy and its interpretation in terms of turbulent convection in the SOL. Section 5 aims at constructing a coherent picture of ELM-averaged power exhaust emerging from the results described in Sections 2 to 4, by considering the interplay between turbulent and collisional transport of plasma thermal energy in the SOL, while drawing a clear distinction between the ion and electron channels. This is accomplished via a systematic analysis of dissipative properties of SOL turbulence. Finally, in Section 6 the main conclusions of the article are briefly summarised and extrapolated from JET to ITER.

There is now ample evidence indicating that radial energy transport is largest in regions of unfavourable magnetic curvature, such that power enters the SOL almost exclusively on the low field, outboard side of the torus. For example, in double null experiments, where the inner and outer scrape-off layers are separated, nearly all the power arrives at the outer divertor [Pitcher97, Stangeby00]. This is observed in both L- and H-mode, and for both inter-ELM and ELM phases of the H-mode [Counsell02, Petrie03]. Such strong in-out asymmetries of energy transport may be linked to the larger outboard area, outward Shafranov shift and bad magnetic curvature of the outboard region; they appears to hold over a wide range of spatial and temporal scales.

As a guideline for the rest of the paper, a schematic of energy flow in the SOL is shown in Fig.1; the meaning of the various mechanisms will be made clear in the course of the discussion. Although this picture applies to both the inter-ELM phase and the ELM transients, the relative magnitude of the channels in these two instances may differ substantially. In the plasmas considered in this study, most of the power enters the SOL during the inter-ELM phase, with an ELM contribution, $P_{ELM}/P_{SOL} = \Delta W_{ELM} f_{ELM}/P_{SOL} \sim 0.2 - 0.4$ where f_{ELM} is the ELM frequency and ΔW_{ELM} the stored energy drop, see Table 1. ELM-averaged power exhaust is therefore composed of a dominant inter-ELM component and a smaller, but still comparable, ELM component. In terms of instantenous power fluxes, the peak ELM values exceed the inter-ELM levels by up to two orders of magnitude.

In the presence of the H-mode transport barrier, with an associated reduction in edge turbulence

and strong temperature gradients in the pedestal region [Parail02], plasma energy enters the SOL mainly by radial collisional diffusion (neo-classical conduction and ion orbit loss effects), i.e. the energy sources are located outside the SOL itself. In contrast, particle sources are spatially distributed in the SOL, due to recycling at the plasma facing components, both divertor and limiter targets. The clear spatial separation between the sources and sinks of energy in the SOL, in contrast to the close interplay of sources and sinks of particles, means that in many ways energy transport poses a simpler, more tractable problem than mass transport, be it for fuel or impurity ions. This is perhaps the key explanation as to why our understanding of the former is quickly outpacing the latter.

The transport of energy in the SOL is an essentially three dimensional process in that it involves three orthogonal directions: parallel$_{||}$, diamagnetic $\wedge$ and radial $\perp$, characterised by the orthogonal unit vectors $e_{||} = b = B/B$, $e_{\wedge}$ and $e_{\perp}$. The $||$ and $\wedge$ directions define the flux surface, and provided the system is axis-symmetric ($\partial/\partial_{\phi} \sim 0$), may be combined into a single, poloidal direction θ with $e_{\theta} = e_{\phi} \times e_{\perp}$ and $e_{\theta} \cdot e_{\perp} = 0$. This simplification does not change the fact that plasma transport occurs in three ($||$, $\wedge$, $\perp$) rather than two (θ, $\perp$) directions. To first order, the radial extent of the SOL and the peak heat loads on the divertor and limiter tiles are governed by competition between $||$ and $\perp$ transport, i.e. between the rapid transport parallel to the magnetic field and the much slower transport perpendicular to the local field; to this order, transport in the diamagnetic $\wedge$ direction mainly affects the in-out asymmetry of the deposited power, i.e. the ratio of power arriving in the inner and outer divertor legs; the relation between in-out asymmetry and $\wedge$ transport is discussed in detail in §3.

A key property of any tokamak equilibrium is the direction of its toroidal magnetic field, and consequently of the vector product $B \times \nabla B$; since ∇B is always directed towards the major axis, this product changes sign upon field reversal. In what follows, we define the forward field (fwd-B or $B \times \nabla B \downarrow$) direction such that $B \times \nabla B$ points towards the X-point (that is down in the case of lower single null plasmas); reversed field (rev-B or $B \times \nabla B \uparrow$) direction is defined such that that $B \times \nabla B$ points away from the X-point. While parallel conduction is largely independent of $B \times \nabla B$ direction, energy and particle transport in the diamagnetic $\wedge$ direction depends on $B \times \nabla B$ through its influence on guiding centre drifts (this point will be made clear in Section 3). As a consequence, SOL flows (both main species and impurity) and divertor asymmetries (density, temperature, pressure, power and radiation) are highly sensitive to the $B \times \nabla B$ direction. For example, the power threshold for the L-H transition is substantially higher with $B \times \nabla B$ away from the X-point, such that it is more difficult to attain the H-mode with a given amount of auxiliary heating [Connor00]. For that reason, most tokamak experiments are performed in fwd-B configurations, which is also the chosen direction for the ITER reference scenario. Therefore, investigation of power exhaust in fwd-B plasmas is clearly the first priority, although operation in rev-B can be extremely useful in advancing our understanding of power exhaust mechanism, eg. role of classical drifts.

The physics of parallel energy transport in the SOL is generally well understood [Stangeby00]; in the collisional regime it is well described by a fluid approximation with

classical Spitzer-Harm-Braginskii heat diffusivities, which in the long mean free path limit are modified with appropriate kinetic corrections, colloquially known as heat flux limits. In contrast, perpendicular transport is generally considered to be anomalous, a historical euphemism suggesting turbulent convection; as was already mentioned, the ITER Physics Basis points out the absence of a reliable theory of perpendicular heat diffusivity [ITER99]. The search for such a theory is the primary motivation behind the work described in this article.

1.2 POWER EXHAUST DIAGNOSTICS ON JET

The JET experiments described below were based on a lower single null, high clearance magnetic configuration with typical inner and outer mid plane wall gaps of ΔR_{in} = 26cm and ΔR_{out} = 16cm, respectively, Fig.2. The main advantage of this configuration is the freedom to slowly shift the plasma as a rigid-body, either vertically or horizontally [Riccardo01, Fundamenski02]. All plasmas are identical in shape, with boundary elongation of ~ 1.7, and upper and lower triangularities of 0.16 and 0.24, respectively. Vertical translation is used to characterise the power deposition profiles on the inner and outer divertors, with strike points located on the lower vertical divertor tiles. Three types of diagnostics are used to measure deposited power profiles on JET divertor targets: Langmuir probes (LP), infra-red thermography (IR) and embedded thermocouples (TC). A detailed discussion of these diagnostics may be found in [Fundamenski04], including their positions in the divertor, Fig.1 of [Fundamenski04].

The TC method, first described in [Riccardo01], involves slowly lifting the plasma as a rigid-body, such that the separatrix strike point passes over the thermocouples embedded in the lower vertical divertor tile. Typically, vertical translations of ~ 15mm/s, lasting 6 seconds are employed during the flat-top phase of neutral beam heated discharges, when plasma conditions remained constant. Finite element modelling of the divertor tile then allows a time-averaged (hence, ELM-averaged) deposited power profile to be extracted. This is done using a variational approach in which the shape of the profile is prescribed as a skewed Gaussian function and its height and width are adjusted until an optimal match to the experimental time trace of the thermocouple is obtained. In this way, the profile of the total deposited power or the heat load on the divertor tile can be calculated. The method has a lower sensitivity limit of ~ 10mm along the target, determined by the depth of the thermocouple beneath the tile surface. Since this is comparable to the narrowest deposited power profile measured on JET, the swept TC method offers an upper limit on the actual ELM-averaged profile width. Note that a relatively long flat top phase is needed for the vertical sweep, which rules out TC measurements of the ELM-free H-mode phase.

Infra-red thermography (IR) on JET was discussed in [Eich03]. This method also measures the total deposited power, but suffers from two major complications: the thermal properties of the tile surface, including reflections of visible light, and finite pixel size of ~ 7mm along the target, which limits profile resolution. On JET, due to the tangentially viewing periscopic system, the latter point is particularly restrictive, with typically only a few pixels per profile. This has been addressed by

measuring the instrument function of the periscope optics using an in-situ black body source. The function was then used to deconvolute the actual profile shape; the resulting TC and IR profiles agree within measurement errors for both L- and H-mode shots. An example for the natural density, Type-I ELMy H-mode case (B_ϕ = 2.5MA, I_p = 2.4T, P_{NBI} = 12MW NBI, unfuelled) is shown in Fig.3, which is adapted from Fig.5 of [Fundamenski04]. The fluxes represent target loads, q_t i.e. energy fluxes per unit area of the divertor target. To convert these to parallel energy fluxes, $q_{||}$ in the plasma, one must multiply by the inclination of the magnetic field lines relative to the target $q_{||}/q_t \sim 1/\sin\theta_\perp$, with $\theta_\perp \sim 3\text{-}5^o$ for plasmas in this study. Profiles are mapped from the distance along the target, s_t to the radial distance upstream (at the outer mid-plane) r_u using a net flux expansion factor, $\Phi = ds_t/dr_u$, which was obtained based on an EFIT reconstruction of the magnetic equilibrium. This factor is found as $\Phi \sim 4$ in the vicinity of the strike point, such that r_u[mm-omp] = s_t[mm-z] / 4, where mm-omp and mm-z indicate the unit mm measured at the outer mid plane and along the target, respectively. The profiles are parameterised in terms of two variables: peak heat flux q_0 and the integral power width, defined as $\lambda_q \equiv \int q dr / q_0$. The latter of can be used to define the near-SOL ($r / \lambda_q < 2 – 3$) and far-SOL ($r / \lambda_q > 2 – 3$) regions, such that plasma power is by definition exhausted primarily via the near-SOL region. Unless otherwise specified, the term SOL will implicitly refer to the near-SOL region.

Figure 1 also shows the power profile obtained by lifting the plasma on a shot-by-shot basis; the deposited profile was then obtained from the change in the ratio of energy deposited on the lower and upper tiles of the outer divertor, as measured by the thermocouples [Matthews01]. Aside from errors in plasma positioning, this is the most accurate measurement method, and indicates that the TC and IR profiles in Fig.3, slightly overestimate the width of the actual ELM-averaged heat load profile. This is consistent with the measurement constraints of both TC (depth of thermocouple ~ 10mm) and IR (pixel size ~ 7mm) methods discussed above.

Finally, divertor Langmuir probes are used to measure the plasma flux, Γ_e and electron temperature, T_e profiles in the divertor. The steady-state electron energy transmission coefficient is relatively insensitive to plasma conditions and may be taken as $\gamma_e \sim 5$ [Stangeby00]. With this assumption the electron parallel power flux into the sheath is computed as $q_{LP} \sim 5T_e\Gamma_e$. It is essential to note that Langmuir probes provide the electron power flux, but offer no information on the ion power flux into the sheath; in other words, $q_{LP} \sim q_e$. Although the collisional assumption $T_i = T_e$ is often invoked to approximate the ion power flux as $q_i \sim \gamma_i T_i \Gamma_e \sim 2T_e\Gamma_e$, it may underestimate the ion power flux under low collisionality conditions, when the ion and electron thermal energies become effectively decoupled. This is the most likely explanation for the difference in magnitude (by a factor of 4 in highest power discharges) between the total (TC or IR) and electron (LP) power fluxes in Fig.3, despite a good match in the shape of all three profiles. In contrast, under lower power, L-mode conditions a good match in both the shape and the magnitude is found (see Fig.2 in [Fundamenski04]). It should be noted that the LP profile in Fig.3, represents only the inter-ELM electron power, i.e. $q_{LP} \sim q_{e,\ \text{inter-ELM}}$. Since the voltage sweeping rate of the Langmuir

probes (100Hz) sets the temporal resolution of the diagnostics at 10ms, while typical ELMs on JET last less than 1ms, the probes cannot measure electron energy flux during the ELM itself. This point will be further discussed in Section 2.

To give a sense of scale, the poloidal gyro-radius $\rho_{\theta i}$ evaluated at the outer mid-plane, which measures the neo-classical banana orbit width ~ $2\rho_{\theta i}$, is also shown in Fig.3; the poloidal field at the outer mid-plane is, of course, larger than the flux surface average, $(B_\theta/B)_{omp}$ ~ 0.3 vs. $\langle B_\theta/B \rangle$ ~ 0.1, due to the ~ 1/R dependence of the toroidal field. The poloidal ion gyroradius in Fig.3 was evaluated for three values of the ion temperature: 100, 300 and 1000eV, which span the range between the top of the pedestal ($T_{i,\,ped}$ ~ 1.1keV) and the upstream separatrix ($T_{i,\,sep}$ ~ 100 - 200eV). The narrow structure in the deposited power profile (~ 2-3mm-omp) is evidently smaller than rqi at the pedestal (~ 6mm-omp) but roughly equal to $\rho_{\theta i}$ at the separatrix (~ 2-3mm-omp). The ratio of poloidal and total gyro-radii is small $(\rho_{\theta i}/\rho_i)_{omp} \sim (B/B_\theta)_{omp} \sim 3$, such that the near-SOL profile width is comparable to the pedestal ρ_i ~ 2mm-omp and only three times larger than the separatrix ρ_i ~ 0.6-1mm-omp. Since ρ_i is the smallest length over which radial variations can exist in a magnetised plasma, this strongly suggests that the dominant radial energy transport process in the near-SOL is close to the lower (laminar) limit set by collisional ion heat conduction. We can therefore expect ion collisions to play an essential role in SOL energy transport, at both the inter-ELM and ELM stages.

2. FORWARD FIELD (FWD-B) EXPERIMENTS: B×∇B TOWARDS THE X-POINT

2.1 EXPERIMENTAL RESULTS

Over the past two years, 22 high clearance discharges dedicated to energy transport have been performed on JET in the forward field direction for a range of conditions [Fundamenski04]. Parameter variation included:

- Neutral Beam Injection power, P_{NBI} from 4 to 18MW
- Additional fuelling rate, with a variation of the Greenwald fraction n/n_{GW} ~ 0.3 - 1
- Toroidal magnetic field, B_ϕ from 1 to 3 Tesla
- Plasma current, I_p from 1.5 to 2.5MA, with a variation of the safety factor, q_{95} ~ 2.6 - 3.8,
- Mass A and charge Z of plasma ions; both deuterium (D) and helium (He) plasmas were studied, with 16D and 6He dedicated discharges. Note that the ratio of mass/charge is the same for He^{++} as for D^+ (A/Z = 2), such that the effects of mass and charge cannot be decoupled.

Both confinement regimes are included in this study with 3 L-mode and 19 ELMy H-mode discharges. In the latter case, most D plasmas involved Type-I ELMs, while He plasmas exhibited the smaller Type-III ELMs; unfortunately, the Type-I ELMy H-mode regime could not be attained in helium plasmas due to lack of sufficient neutral beam heating power (He^0 injection was used). There was no additional fuelling during the H-mode phase in most discharges, producing the so-called natural density H-mode operation, in which the plasma density is determined by particle recycling alone. A detailed analysis of these experiments may be found in [Fundamenski04]; below

we briefly revisit this analysis in the light of more recent results.

The peak heat loads on the outer divertor, both total q_{tot} (TC) and electron q_e (LP), are shown in Fig.4, where they are plotted vs. the total power to the outer target P_t (TC); this figure is adapted from Fig.3 of [Fundamenski04]. Inner target heat loads are not shown as these are smaller by a factor of five; we will return to the issue of in-out asymmetry in the following section. The results are divided into D and He plasmas, and only unfuelled (natural density) H-mode discharges are shown; for reference, the L-mode points are also indicated. For D plasmas, $q_{tot} \approx q_e + q_i$ increases faster than linearly with input power, indicating that the SOL power profile becomes narrower with P_t, since $\lambda_q \propto P_t / q_{tot}$. It also begins to greatly exceed the electron peak heat load q_e as measured by LP, which increases slower than linearly with P_t; this discrepancy (excess heat load) between the total and electron values was already noted in connection with Fig.3. We may interpret this excess heat load as the upper limit on the net ion heat load, $q_i = q_{i,\ inter\text{-}ELM} + q_{i,\ ELM}$, defined as the sum of inter-ELM and ELM ion contributions (assuming of course an ion distribution function with $T_i > T_e$), which may be written as

$$q_{tot} - q_{e,\ LP} \sim q_{tot} - q_{e,\ inter\text{-}ELM} \sim q_{i,\ inter\text{-}ELM} + q_{i,\ ELM} + q_{e,\ ELM} > q_i \sim 2T_i\Gamma_i.$$

The neglect of charge-exchange neutrals and radiation is justified by the fact that these mechanism are a factor of 100 too small to account for the excess peak heat loads. On the other hand, the role of energetic particles (both ions and electrons) associated with ELMs is made explicit in the above formulation. The difference between the excess heat load $q_{tot} - q_{e,\ LP}$ and the ion contribution q_i, is thus the unknown electron ELM heat load $q_{e,\ ELM}$. While this quantity cannot be diagnosed at present, kinetic simulations indicate that the electron contribution to the ELM deposited power is typically less than 50%, and may be as little as 20%, i.e. $P_{e,\ ELM} / (P_{i,\ ELM} + P_{e,\ ELM}) \sim 0.2 – 0.4$ [Bergmann02]. Since the electron pulse during the ELM is deposited more promptly than the ion pulse, we expect the electron contribution to the peak heat load to be somewhat larger. With ELMs responsible for roughly a third of the power crossing the separatrix in these shots, $P_{e,\ ELM}$ amounts to < 15% of P_{SOL}. Thus, to first order we may identify the excess power with the ion contribution.

The decoupling of ELM and inter-ELM components is additionally complicated by the fact that ELMs do not appreciably broaden divertor power profiles (at most by a factor of 2) with respect to their inter-ELM values [Herrmann03]. The presence of Type-III ELMs in helium plasmas further complicates the issue, Fig.4. It may thus be argued that excess heat flux $q_{tot} - q_{e,\ LP}$ observed for high power deuterium H-modes, is simply a remnant of the larger type-I ELMs; in helium plasmas, in which only the smaller Type-III ELMs are found, this excess $q_{tot} - q_{e,\ LP}$ is indeed very small, Fig.4. In the absence of Type-I ELMy H-mode helium data, this point cannot be conclusively resolved. As a result, it is difficult to decouple the inter-ELM and ELM contributions as has been indicated in the schematic of Fig.1. This caveat will be implicit whenever the ion and electron powers are mentioned below.

The separatrix ion collisionality, $\nu_i^* \equiv L_{||}/\lambda_{ii} \propto L_{||} n/T_i^2$, where $L_{||}$ is the connection length and λ_{ii} is the ion-ion collisional mean free path, emerges as the governing parameter for the excess peak heat load on the outer target $q_i \sim q_{tot} - q_{e,\,LP}$. This is indicated by Fig.5, where $q_{tot}/q_{e,\,LP}$ is plotted vs ν_i^*. While electrons remain collisional ($\nu^*_e \equiv L_{||}/\lambda_{ee} > 30$) in all cases considered, ions become progressively less collisional with input power, down to the levels of marginal collisionality in high power, unfuelled, deuterium Type-I H-modes ($\nu^*_i < 3$); the cubic dependence of the collisionality on the ion charge is responsible for the high values of ν^*_i in helium discharges. Both collisionalities were calculated using the two-point model estimates of upstream temperatures and density, $T_{e,\,u}$, $T_{i,\,u}$ and $n_{e,\,u,}$ [Stangeby00], based on target LP measurements of $T_{e,\,t}$ and $n_{e,\,t,}$ and the peak target heat flux q_{tot}. Based on the $q_i \sim q_{tot} - q_{e,\,LP}$ assumption, the inferred ion temperature at the outer target is ~ 300eV at lowest collisionality [Fundamenski02]. Carbon ion temperature profiles, measured by charge-exchange resonance spectroscopy, indicate that T_i^{C6+} varies slowly in the pedestal region, with $T_{i,\,sep}^{C6+} \sim 0.8 T_{i,\,ped}^{C6+} \sim 700$eV [Andrew04]. Provided $T_i^{D+} \sim O(T_i^{C6+})$, the inferred target T_i and the estimated separatrix T_i^{D+} are comparable, then the hot target ions originate close to, within one poloidal gyro-radius of, the separatrix.

It should be noted that unlike Fig.4, which contains only unfuelled H-modes, Fig.5 also includes additionally fuelled H-modes. This shows that the beneficial effect of fuelling in reducing the peak heat load occurs by increasing the ion collisionality. Since high collisionality implies strong coupling between ion and electron channels, we expect $T_i \sim T_e$ and hence $q_{e,\,LP} \sim q_{tot}$ under collisional conditions. This is in fact observed in Fig.5, where for $\nu_i^* > 10$, the electron and total peak heat loads are nearly equal ($q_{tot}/q_{e,\,LP} \sim 7/5$) as expected from sheath physics, which for $T_i \sim T_e$, predicts $q_{tot} \sim q_i + q_{e,\,LP} \sim 7 T_e \Gamma_e$ and $q_{e,\,LP} \sim 5 T_e \Gamma_e$. Under collisionless conditions ($\nu_i^* < 5$), the ratio $q_{tot}/q_{e,\,LP}$ increases above unity and the ion heat flux begins to dominate, Fig.5. As shown in the figure, this ratio is strongly correlated with the steepening of the power profile measured by q_{tot}/q_{base}, where q_{base} is the peak heat load extrapolated from the far-SOL (base) profile, i.e. the excess (ion) contribution determines the integral width of the near-SOL power profile. In JET H-mode discharges this width has been found to scale as

$$\lambda_q^{all} \propto A^{\alpha} Z^{\beta} B_{\phi}^{-1.03} q_{95}^{0.6} P_t^{-0.41} n_{e,\,u}^{0.25},\ \alpha + \beta = 1.04 \qquad (2.1a)$$

if all discharges are included, and

$$\lambda_q^{H} \propto A^{\alpha} Z^{\beta} B_{\phi}^{-0.93} q_{95}^{0.41} P_t^{-0.48} n_{e,\,u}^{0.15},\ \alpha + \beta = 1.11 \qquad (2.1b)$$

if only H-mode shots are retained [Fundamenski04]; the 0.95 flux surface index is included to differentiate the safety factor from the heat flux, both of which are denoted by q. Both of the scalings (2.1a) and (2.1b) are dominated by natural density H-modes under attached conditions.

2.2 THEORIES OF RADIAL ENERGY TRANSPORT

In order to determine the mechanism of radial energy transport in the SOL, the experimentally obtained scalings (2.1) have been compared with the predictions of all available theories of radial heat transport. The collection of theories and their labelling are essentially borrowed from [Connor99]. The interested reader is referred to that study and the citations contained therein, for a detailed description of the underlying physics of each theory. The scaling of the heat diffusivity $\chi_\perp$ with A, Z, B_ϕ, q_{95}, n_e and T_σ and λ_q, predicted by individual theories is summarised in Table 1 of [Fundamenski04]. In addition, several theories for λ_q and $\chi_\perp$ not considered in [Connor99] have also been included in the comparison, involving the collisionless radial lengths:

- **Y1**: ion gyro-radius, $\rho_i \propto A^{0.5}Z^{-1}B^{-1}T_i^{0.5}$
- **Y2**: poloidal ion gyro-radii, $\rho_{\theta i} \sim \rho_i(B/B_\theta) \propto A^{0.5}Z^{-1}B_\theta^{-1}T_i^{0.5}$
- **Z1**: electron gyro-radius, $\rho_e \propto B^{-1}T_e^{0.5}$ the footprint of direct ion orbit loss on the outer divertor target,
- **X**: direct ion orbit loss, λ_q^X, see (2.2) below and collisional heat diffusivities,
- **A1**: classical ion heat conduction, $\chi_\perp^{A1} \propto \rho_i^2\nu_i$
- **A2**: neo-classical ion heat conduction, $\chi_\perp^{A2} \propto \chi_\perp^{A1}(B/B_\theta)^2 \propto \rho_{\theta i}^2\nu_i$
- **A3**: classical electron heat conduction, $\chi_\perp^{A3} \sim \chi_\perp^{A1}(m_e/m_i)^{1/2} \propto \rho_e^2\nu_e$

where ν_i and ν_e are the characteristic ion and electron collision frequencies. Because of their importance in what follows, a brief discussion of these theories is appropriate. The role of the ion and electron gyro-radii was already mentioned in the context of Fig.3; they determine the smallest possible radial variation of the ion and electron distribution function, respectively.

Ion orbit loss (IOL) is a well known transport mechanism in diverted tokamak plasmas [Shaing89]; it can be accurately described as neo-classical transport in the presence of the X-point, and involves the opening out of the ion banana orbits by the change in the field topology in the vicinity of the separatrix. The loss orbits then terminate at either the inner or the outer divertor target, assuming the radial distance to the limiter exceeds 2 – 3 poloidal gyro-radii. The topology of the loss orbits and hence the in-out loss asymmetry is therefore highly sensitive to the direction of the B×∇B drift, which determines the sense of poloidal rotation of the guiding centre in the banana orbit. In the past, ion orbit loss has been suggested as a possible explanation of both the L-H transition [Shaing89] and narrow structures in deposited power profiles [Lingertat97, Fundamenski02].

The effect of field reversal on ion orbit loss is illustrated in Fig.2, which shows the results of a calculation using the guiding centre Monte-Carlo code ASCOT [Heikkinen01]. The magnetic equilibria used in the simulations were reconstructed using EFIT for the matching fwd-B and rev-B pulses, 50415 and 59589 in Table 1. The initial ion launch location is labelled dark grey (blue) if the orbit terminates at the inner target and light grey (red) if it strikes the outer target. In the fwd-B direction, Fig.2(a), the outer launch orbits terminated mostly on the outer target, and the inner launch at inner target. The situation is reversed in rev-B direction, Fig.2(b), where the outer orbits terminate at the inner target and vice versa. It is evident that the out-in asymmetry of direct ion orbit

losses is highly sensitive to the B×∇B direction.

For typical JET H-mode conditions, ions lost from the top of the pedestal effectively follow direct, collisionless orbits in the SOL ($\nu^*_{i,\,ped} < 1$), while those lost close to the separatrix suffer multiple collisions in the SOL ($\nu^*_{i,\,sep} > 1$). It is therefore useful to draw a distinction between direct ion orbit loss, in which collisions only play a role in the pedestal region (i.e. in the generation of the scattering of ions onto lost orbits), and collisional ion orbit loss, in which collisions in the SOL significantly modify the trajectory leading to diffusive radial broadening. This distinction was made explicit in Fig.1, where only direct IOL bypasses the thermal ion population in the SOL. Earlier studies showed that the observed JET outer target profiles could be explained by direct ion orbit loss, provided rather large values of the radial electric field in the SOL ($E_r^{SOL} \sim$ 30-50kV/m) were assumed [Fundamenski03]. These conclusions were based on simulations of ion orbit loss using the guiding centre Monte-Carlo code ASCOT [Heikkinen01] in realistic JET geometry with reconstructed edge and SOL plasma and neutral profiles [Fundamenski02]. Nevertheless one important feature of these simulations was the assumption of sharp pedestal profiles, such that all particles were launched with pedestal energies and therefore the SOL plasma did not significantly broaden the orbits. Hence, despite the inclusion of SOL plasma and neutrals, the simulated process constituted only direct ion orbit loss. Over thirty ASCOT simulations were performed with $1.5T < B_\phi < 3.5T$, $2.6 < q_{95} < 5.2$, $3m < R < 6m$, $A \leq 12$ and $Z \leq 2$, to calculate the footprint of direct ion orbit loss on the outer divertor target in the forward field direction. The result is the following scaling for target power width [Fundamenski04]:

$$\lambda_q^X = 2.2 \times A^{0.35\pm0.03}\, Z^{-0.8\pm0.06}\, Bf^{-0.89\pm0.04} q_{95}^{0.88\pm0.04} T_{i,\,ped}^{0.39\pm0.1} n_{e,\,ped}^{-0.08\pm0.1} (R/3)^{0.8\pm0.1} \quad (2.2)$$

where λ_q^X is in mm-omp, B_ϕ the on-axis toriodal field in Tesla, R is the major radius in meters, $T_{i,\,ped}$ the ion pedestal temperature in keV, and $n_{e,\,ped}$ the pedestal density in 10^{20} m^{-3}. We note that $\lambda_q^X \sim L_{||}^{0.85}$, when the R and q_{95} scalings are combined. Not surprisingly, λ_q^X scales roughly as the poloidal gyro-radius $\rho_{\theta i}$, i.e. as the banana width. The minor difference can be explained by topological effects associated with the X-point and collisions with the SOL background plasma and neutrals. At this stage, the scaling with SOL density and temperature has not been not properly assessed, but such a study is envisioned in the future.

The final three theories (A1, A2, A3) involve collisional transport. A modern account of collisional transport in magnetised plasmas, generally referred to as classical and neo-classical transport, including a derivation of the corresponding radial heat diffusivities, may be found in [Helander02]. The terms classical and neo-classical refer to the cylindrical ($\varepsilon \equiv r / R \to 0$) and toroidal ($\varepsilon > 0$) geometries respectively. In both cases, radial heat conduction can be approximated as a diffusion process with a radial step taken as the gyro-radius and step time as the collision frequency, i.e. $\chi_{\perp\sigma} \propto \rho_\sigma^2 \nu_\sigma$ where $\sigma \in \{i,e\}$. Since the gyro-radius is much larger for ions than for electrons, on account of their larger mass, collisional heat conduction is also much faster for these species. In this

approximation, classical and neo-classical transport differ mainly in their radial step size, with $\rho_{\theta i}$ taking the role of ρ_i, and enhancing the classical $\chi_{\perp i}$ by a factor ~ $(\rho_{\theta i}/\rho_i)^2 \sim (B/B_\theta)^2$. The above picture neglects the role of collisionality, $\nu^*_i \sim Rq_{95}/\nu_{ii}$. When it is included, three separate neo-classical transport regimes may be distinguished, which in order of increasing ν^*_i, are known as banana, plateau and Pfirsch-Schlueter regimes. In practice, the intermediate (plateau) regime disappears for $\varepsilon > 0.2$, relevant to the edge plasma, such that neo-classical transport can be effectively divided into the low collisionality ($\nu^*_i < 1$), banana regime and the high collisionality ($\nu^*_i > 1$), Pfirsch-Schlueter regime [Helander02]. In the former, the collision frequency is much smaller than the transit, or bounce frequency of the banana orbit, and the simple diffusive picture with radial step size $\rho_{\theta i}$ applies; the only modification is a factor $f_t \sim 1.5\varepsilon^{1/2}$ ($f_t \sim 0.85$ for $\varepsilon \sim 1/3$), representing the fraction of trapped (banana) particles in the total ion population, such that $\chi_\perp^{A2} \sim 1.5\varepsilon^{1/2}\rho_{\theta i}^2\nu_{ii} \sim (B/B_\theta)^2\chi_\perp^{A1}$.

This regime is unlikely to exist in the SOL for two reasons: 1) as already mentioned, the effect of the X-point leads to the opening out of banana orbits, i.e. to ion orbit loss, 2) ion collisionality in the SOL exceeds unity, $\nu^*_i > 1$, cf. Fig.5. Consequently, neo-classical transport in the SOL should be in the Pfirsch-Schlueter regime, in which the ion orbit is frequently interrupted by ion-ion collisions. This leads to a highly asymmetrical radial heat flux, with an outflow of heat on the outboard, low field side and an inflow on the inboard, high field side, changing sign at the top and bottom of the torus, $\chi_\perp^{PS} \sim 1.6q_{95}^2[\varepsilon^{-1}\cos\theta + O(1)]\chi_\perp^{A1}$, where q is the poloidal angle ($\theta = 0$ at the outer mid-plane). When averaged over the flux surface, the two large contributions cancel to the highest order in ε, leaving a difference of order ε^2. This results in the enhancement of the flux surface averaged value of the heat diffusivity with respect to the classical value by a factor of $1.6q_{95}^2$ where $q_{95} \sim \langle \varepsilon B/B_\theta \rangle_{95}$ is the average safety factor on the 0.95 flux surface. The final diffusivity can be written as $\chi_\perp^{A2} \sim 1.6q_{95}^2\chi_\perp^{A1} \sim 1.6\varepsilon^2\langle B/B_\theta\rangle^2\chi_\perp^{A1}$. Due to the presence of the X-point and the opening of flux surfaces in the SOL, the above estimate of the Pfirsch-Schlueter diffusivity obtained for closed flux surfaces could be significantly modified in the SOL. Nonetheless, this value should serve for the purpose of the cross-theory comparison.

In JET discharges considered here, $\varepsilon \sim 1/3$ and $q_{95} \sim 2.6$ are typical, such that the flux surface average $\langle B/B_\theta \rangle_{95} \sim 8$; this should be compared with the outer mid-plane ratio of $(B/B_\theta)_{omp} \sim 3$ obtained from the EFIT reconstruction. Consequently, the banana and Pfirsch-Schlueter enhancement factors, $0.85(B/B_\theta)^2_{omp} \sim 8$ and $1.6q_{95}^2 \sim 11$, respectively, are roughly equal provided the former is evaluated at the outer mid-plane. In addition, for a plasma of fixed size, such that ε = constant, both the banana and Pfirsch-Schlueter heat diffusivities scale identically with plasma and field variables; for this reason we do not distinguish between these regimes, but retain only the generic neo-classical form, $\chi_\perp^{A2} \propto \chi_\perp^{A1}(B/B_\theta)^2 \propto \chi_\perp^{A1}q_{95}^2$.

We close this brief discussion by ordering the theories of radial heat diffusivity in the SOL in

terms of increasing complexity:

- **Q**: $\chi_\perp$ = constant,
- **Y, Z**: collisionless ($\lambda_q \sim \rho_\sigma, \rho_{\theta\sigma}$),
- **X**: direct ion orbit loss ($\lambda_q \sim \lambda_q^X$)
- **A**: collisional diffusion ($\chi_\perp$ ~ classical, neo-classical)
- **B-O**: turbulent (MHD interchange, drift-Alfven), charge-exchange and ad hoc

2.3 COMPARISON OF EXPERIMENTAL RESULTS VS. THEORETICAL PREDICATIONS

In order to perform the comparison for such a large number of theories, the power width λ_θ was related to $\chi_\perp$ using a simplified diffusive model of SOL energy transport, Appendix A of [Fundamenski04],

$$\lambda_q \sim (\chi_\perp \tau_{||})^{1/2}, \quad \tau_{||}^{-1} \sim \tau_{||v}^{-1} + \tau_{||\chi}^{-1}, \quad \tau_{||} v \sim L_{||}/c_s, \quad \tau_{||}\chi \sim L_{||}^2/\chi_{||} e \qquad (2.3)$$

where $\tau_{||v}$ and $\tau_{||\chi}$ are the convective and conductive energy loss times, respectively, and $\tau_{||}$ is the harmonic average of the two. While the magnitude of $\lambda_q(\chi_\perp)$ in this estimate is at best valid to within a factor of two, its scaling with plasma, field and ion variables should be captured to a much higher accuracy. This was in fact demonstrated by comparing λ_q in the limits of conductively and convectively dominated parallel transport, $\lambda_q^v = \lambda_q(\tau_{||v})$ and $\lambda_q^\chi = \lambda_q(\tau_{||\chi})$, respectively. The comparison showed that the scaling of $\lambda_q(\chi_\perp)$ was insensitive to the details of parallel transport. In addition, the diffusive estimate (2.3) was successfully validated under attached plasma conditions against the 2-D fluid transport code EDGE2D [Fundamenski04].

The error between the theoretical prediction and experimental λ_q scaling is shown as a bar chart, where each bar represents a single theory and different shades represent contributions from different exponents in the scaling, Fig.6 (or Fig.6(c) of [Fundamenski04]). The figure suggests that three collisional theories (classical ion **A1** and electron **A3** conduction and neo-classical ion conduction **A2**) give the best match to the experimental data, with **A1** a clear favourite, it being the only theory to satisfy the diagnostic error margin indicated by the dot-dashed line [Riccardo01]. If only the well known quantities Z(A), B, q_{95} are considered (the estimates of upstream density and temperature values carrying significant error bars), the agreement between this theory and the experiment is even more startling. In short, the best three theories all involve laminar (non-turbulent), collisional transport with a strong indication that classical ion conduction predominates. The collisional theories are followed by Bohm (**N**), endplate MHD interchange (**B2**, **G2**), change exchange (**M**) and the null model, $\chi_\perp$ = constant (**Q**).

The calculated footprint of direct ion orbit loss (2.2), which roughly follows the poloidal ion gyro-radius $\lambda_q^X \sim \rho_{\theta i}$, is in very poor agreement with the observed scalings of A(Z), B_ϕ and q_{95} (theory **X** in Fig.6). We will see presently, however, ion orbit loss combined with ion-ion collisions in the SOL, that is collisional ion orbit loss, offers excellent agreement with experiment.

The above conclusions, based on the scaling of λ_q with plasma, field and ion variables, are reinforced by consideration of the magnitude of λ_q. This is found to lie between classical **A1** and neo-classical (Pfirsch-Schlueter) collisional **A2** predictions, but greatly exceeds the classical electron collisional **A3** prediction,

$$\lambda_q \sim 2.2\times\lambda_q^{\mathbf{A1}} \sim 0.6\times\lambda_q^{\mathbf{A2}} \sim 21\times\lambda_q^{\mathbf{A3}} \qquad (2.4)$$

The ion collisional widths in (2.4) assume parallel convective losses at the upstream sound speed, $\lambda_q \sim (\chi_\perp \tau_{\|v})^{1/2}$, a fair approximation under low collisionality conditions, which leads to $\lambda_q^{\mathbf{A1}} \sim (\rho_i^{\,2}\nu_{ii}L_\|/c_s)^{1/2} \sim \rho_i \nu^*_i{}^{1/2}$ and $\lambda_q^{\mathbf{A2}} \sim (\rho_{\theta i}^{\,2}\nu_{ii}L_\|/c_s)^{1/2} \sim \rho_{\theta i} n^*_i{}^{1/2}$; the reduction makes use of $\nu_{ii}L_\|/c_s \sim \nu_{ii}L_\|/v_{ti} \sim L_\|/\lambda_{ii} \sim \nu^*_i$. In contrast, the electron collisional width assumes parallel electron conduction, which is more appropriate to electron energy loss. Thus $\lambda_q \sim (\chi_\perp \tau_\| \chi)^{1/2}$, as also defined in (2.3), such that $\lambda_q^{\mathbf{A3}} \sim (\rho_e^{\,2}\nu_{ee}L_\|^{\,2}/\chi_{\|e})^{1/2} \sim \rho_e \nu^*_e$; here $\nu_{ee}L_\|^{\,2}/\chi_{\|e} \sim \nu_{ee}L_\|^{\,2}/v_{te}\lambda_{ee} \sim L_\|^{\,2}/\lambda_{ee}^{\,2} \sim \nu^*_e{}^2$. The appearance of the collisionalities ν^*_σ in both expressions is indicative of a random walk, diffusive process.

The classical and neo-classical power width predictions, obtained above, involve only collisional transport; they implicitly assume that the background plasma flow is quiescent or laminar, and therefore represent the narrowest possible profiles likely to exist in the SOL under given upstream conditions. For future reference, we note that they are also the long wavelength (two dimensional) limit $k_\| \to 0$ of the turbulent dissipative scales, which will be discussed at length in §5. Under these conditions, the electron power width is roughly an order of magnitude smaller than the ion power width, due to the smaller electron $\chi_{\perp e} << \chi_{\perp i}$ and faster $\chi_{\|e} >> \chi_{\|i}$.

With this in mind, a number of important conclusions can now be drawn from (2.4). First, the observed power profile is much broader than would be expected from the purely laminar approximation, that is $\lambda_q >> \lambda_q^{\mathbf{A3}}$; if we take the range of observed electron profiles as set by the near-SOL and far-SOL values, $\lambda_q^{\,e} \sim (1\text{-}2)\lambda_q$, then the observed to classical ratio becomes $\lambda_q^{\,e}/\lambda_q^{\mathbf{A3}} \sim 20\text{-}40 \sim O(30)$. This alone implies the presence of turbulence in both the near- and far-SOL regions! Expressing the level of turbulence as an effective radial heat diffusivity, which from (2.3) can be written as $\chi_{\perp e} \sim \lambda_q^{\,2}/\tau_{\|\chi}$, we obtain $\chi_{\perp e}/\chi_\perp^{\mathbf{A3}} \sim (\lambda_q^{\,e}/\lambda_q^{\mathbf{A3}})^2 \sim O(10^3)$, so that turbulent convection entirely determines the radial electron energy transport.

Secondly, the total power profile is comparable to the laminar ion approximation, for both classical and neo-classical expressions: that is, $\lambda_q \sim 2\lambda_q^{\,A1} \sim 0.5\lambda_q^{\,A2}$. If we interpret the narrow near-SOL profiles as an ion contribution, $\lambda_q \sim \lambda_q^{\,i}$, than the effective radial heat diffusivity $\chi_{\perp i} \sim \lambda_q^{\,2}/\tau_{\|v} \sim 0.01 - 0.05\ m^2 s^{-1}$ is comparable to the collisional estimate, $\chi_{\perp i} \sim 4\chi_\perp^{\mathbf{A1}} \sim \chi_\perp^{\mathbf{A2}}/4$. These values only apply in the near-SOL, and increase to much higher levels up to $1\ m^2 s^{-1}$ in far-SOL. This was first noted in [Fundamenski01], where the radial diffusivity profile was extracted for a JET high power H-mode using the fluid transport code OSM2/EIRENE, and compared with classical and neo-classical estimates; the result was $\chi_{\perp i} \sim O(\chi_\perp^{\mathbf{A2}})$ close to the separatrix. We may conclude that

while some level of turbulence is evidently present in the near-SOL, and dominates particle, momentum and electron energy transport, it is far less important for ion energy transport on account of the larger ion collisional diffusivity – essentially, an instance of the so-called finite Larmor radius effect, in which $f_i(\mathbf{x}, \mathbf{v})$ is smoothed radially by ion gyration over the radial extent of ρ_i. We will return to this important point in §5.

To obtain a collisional ion orbit loss width, we make use of the discussion following (2.4) and take the direct ion orbit loss width lqX on the outer divertor plate (2.2) as the diffusive step size with step time ν_{ii}^{-1} to obtain $\chi_\perp^{X} \sim (\lambda_q^{X})^2 \nu_{ii}$. Assuming $\lambda_q^{X} = \lambda_q^{X}(\tau_{\|v})$, we arrive at the following expression for the collisional ion orbit loss width,

$$\lambda_q^{\mathbf{X}-\nu^*} = \lambda_q^{\mathbf{X}} \nu^*{}_i^{1/2} \tag{2.5}$$

An alternative, more ad hoc formulation, involves a transitional expression between $\lambda_q^{\mathbf{A1}}$ and $\lambda_q^{\mathbf{X}}$,

$$\lambda_q^{\mathbf{A1\text{-}X}} = 2.4\xi\lambda_q^{\mathbf{A1}} + (1\text{-}\zeta)\lambda_q^{\mathbf{X}}, \tag{2.6}$$

where $\zeta \equiv \nu^*_i / (1 + \nu^*_i)$ approaches zero for collisionless and unity for collisional conditions, and the factor 2.4 was chosen to best fit the available JET data. Both expressions offer excellent fits, within the experimental error of 20%, to the measured power widths, $\lambda_q \sim \lambda_q^{\mathbf{X}\text{-}\nu^*} \sim \lambda_q^{\mathbf{A1\text{-}X}}$.

The magnitudes of all collisional predictions, including the collisional ion orbit loss estimates (2.5) and (2.6), measured power widths are compared in Fig.7, where the poloidal gyro-radius evaluated at the upstream separatrix is also shown. Within the accuracy of the estimate, fair agreement is found with all collisional estimates, although the collisional ion orbit loss expressions (2.5) and (2.6) give the best match to the data. These values are intermediate between the classical ($\varepsilon = 0$, $\chi_{\perp i} \sim q_{95}^{0}$) and neo-classical ($\varepsilon > 0$, $\chi_{\perp i} \sim q_{95}^{2}$) predictions, suggesting that ion transport in the near-SOL involves aspects of both regimes and may scale as $\chi_{\perp i} \sim q_{95}^{k}$ where $0 < k < 2$. We will henceforth refer to this intermediate transport regime as (neo-)classical. Since this regime spans the range set by classical and neo-classical limits, it includes such effects as collisional ion orbit loss which is behind the best fit expressions (2.5) and (2.6). Based on both scaling and magnitude comparison, we can conclude that (neo-)classical transport offers the best match to JET data in the fwd-B direction.

3. REVERSED FIELD (REV-B) EXPERIMENTS: B¥—B AWAY FROM THE X-POINT

In order to further discriminate between direct ion orbit loss and (neo-)classical ion conduction – only the former being sensitive to the B×∇B direction – dedicated reversed field experiments were recently performed on JET [Pitts05, Fundamenski05]. The idea of reversing the magnetic field in a tokamak is not new. Such experiments have been performed in the past on nearly all machines, including JET [Chankin97]. However, much of this earlier work is concerned with ohmic or

L-mode plasmas, with a focus on low power, high density regimes [Hutchinson95, Pitcher97, Stangeby00]. In light of the low $\nu^*_{i,sep}$ in ITER and recent improvements in divertor thermography, it was felt that new JET experiments providing closely matched forward-reversed pairs of H-mode discharges were desirable. To provide compatibility with fwd-B experiments, the same high clearance magnetic configuration was used. Both B_ϕ and I_p were reversed, such that the magnetic helicity remained constant. The deposited power profiles on the inner and outer divertors were measured using the same techniques as for the fwd-B experiments (see Section 1).

3.1 EXPERIMENTAL RESULTS

Four good discharges, forming fwd-B/rev-B matched pairs were obtained, one L-mode and three H-modes at different values of B_ϕ, I_p and P_{NBI}; these are summarised in Table 1. The discharges are fairly well matched in terms of power entering the SOL, $P_{SOL} = P_{heat} - P_{rad}$, i.e. heating minus core plasma radiative powers and volume averaged density $<n_e>$; the majority 60 – 90% of this power crosses the separatrix during the inter-ELM phase as observed from the ratio P_{ELM}/P_{SOL}. However, the ELMs are typically smaller and more frequent in rev-B discharges, with $\Delta W_{ELM}/W_{ped}$ ranging from 4 – 9% in fwd-B to 1 – 5% in rev-B. Note that Type-I ELMy H-mode could not be obtained at 2.5MA/2.4T with 14MW of NBI heating due to the higher III-I power threshold in rev-B [Andrew04].

Due to progressive wiring failure, the LP coverage was much poorer at the time of the reversed field experiments, hence the ~ sign in Table 1 denoting errors of order ± 50% in the saturatiion current, js and electron temperature, T_e. Nonetheless, it is clear that the inner target T_e is nearly doubled by field reversal (from ~10eV to ~20eV), while the outer T_e remains in the range ~20-30eV. The trends in j_s and T_e are discussed in more detail in [Fundamenski05]. The upstream values of density and temperature, n_e^{SOL} and T_e^{SOL}, and were predicted using a two-point model estimate based on total (TC) heat fluxes to the outer target.

The TC-measured, ELM-averaged deposited heat load profiles for the matched pairs of shots of Table 1 are shown in Fig.8, along with total deposited powers P_t, peak values q_{peak} and integral widths λ_q. The resulting out-in deposited power asymmetry P_o/P_i is reduced from ~ 2.65 – 2.2 for fwd-B to ~ 1.7 – 1.9 for rev-B, with the average value roughly constant at 2.1±0.05. This asymmetry increases roughly linearly with power into the SOL, P_{SOL}, with a weaker slope for H-mode plasmas. Similar behaviour was observed on a large sample (>100 shots) of unmatched fwd-B and rev-B JET plasmas from the same experimental campaign [Pitts05]. Furthermore, based on matched fwd-B and rev-B L-mode discharges (2.0MA, 2.4T, P_{NBI} ~ 2 – 8MW) with detailed radiation accounting using tomographic reconstructions of bolometric lines of sight [Huber05], shows that target power asymmetries reflect actual changes of power flux into the divertor legs $P_{div} = P_t + P_{rad,\,div}$ ($P_{div,\,o}/P_{div,\,i}$ ~2.3 for fwd-B vs. ~1.3 for rev-B), rather than simply asymmetry in divertor radiation, as suggested by a recent review [Pitcher97]. In other words, a significant poloidal component of the SOL energy flux was shown to depend on the $\mathbf{B}\times\nabla B$ direction, in line with conclusions reached on the basis of reversed field experiments in Alcator C-Mod [Hutchinson95].

The out-in peak heat flux asymmetry in Fig.8 and Table 1 (both TC and LP) ranges from 5 – 7 for fwd-B, and 1.7 – 3.7 for rev-B. Although not shown in Fig.8, the ratio of total to electron power in H-mode, which for fwd-B is in the range 2 – 5, is reduced in rev-B to 1.2 – 1.8. If, as before, we attribute the excess power to the ions, this suggests the field dependent poloidal energy flux in the SOL needed to explain the power asymmetries, is mainly carried via the ion channel.

3.2 COMPARISON OF FWD-B AND REV-B RESULTS

To asses the role of field reversal on radial energy transport, the above peak heat load values are plotted in Fig.9 (or Fig.3 of [Fundamenski05]) vs. the fwd-B scaling $q_t \sim P_t/\lambda_q$ with λ_q given by (2.1a). Within the measurement errors, the outer target rev-B H-mode points do not substantially differ from the fwd-B scaling, while the inner target and L-mode points are only grossly correlated with the scaling. We conclude that under low collisionality (attached) conditions, the power width lq is insensitive to the $\mathbf{B}\times\nabla$B direction. Since this quantity is directly related to the radial ($\perp$) heat diffusivity, $\lambda_q \sim (\chi_\perp \tau_{||})^{1/2}$, we infer that radial energy transport in the SOL is largely independent of the $\mathbf{B}\times\nabla$B direction, i.e. the $\mathbf{B}\times\nabla$B direction affects the poloidal (θ) but not the radial ($\perp$) energy transport. This observation suggests the role of poloidal classical drifts [Schaffer97, Chankin97], which we will address below.

As has already been noted, power enters the SOL primarily on the low field side of the torus, irrespective of the $\mathbf{B}\times\nabla$B direction. This can be explained by: a) larger outboard area, b) Shafranov shift compressing the outboard flux surfaces, c) bad curvature leading to MHD interchange instabilities and driving turbulence on the low field side. The curvature effect is evident in the observed asymmetry of neo-classical ion conduction in the Pfirsch-Schlutter regime, §2; the ion heat flux is outwards on the low field side and inward on the high field side: $q_{\perp i}^{PS} = -\chi_{\perp i}^{PS}\nabla_\perp T_i$ where $\chi_{\perp i}^{PS} \sim 1.6q_{95}^2[\varepsilon^{-1}\cos\theta + O(1)]\chi_\perp^{A1}$, with $\theta = 0$ at the outer mid-plane. These effects, together with shorter connection length from the outer mid-plane to the outer target, $R_o/R_i \sim L_{||i}/L_{||o} \sim 2$ predict an average out-in power asymmetry of ~ 2, in fair agreement with the experimental value of 2.1±0.05.

The change of the out-in power asymmetry with field reversal implies a B×∇B dependent poloidal energy transport. The origin of this effect may be explained in terms of classical (guiding centre and diamagnetic drifts) which leads to a net energy flux [Helander02, Chankin97],

$$\mathbf{q}_\sigma \approx 2.5p_\sigma\mathbf{u}_\sigma + 2.5p_\sigma v_{t\sigma}\rho_\sigma\mathbf{b}\times\nabla T_\sigma/T_\sigma, \qquad \sigma\in\{i,e\} \tag{3.1}$$
$$\mathbf{u}_\sigma = u_{||\sigma}\mathbf{b} + \mathbf{v}_E + \mathbf{b}\times(\nabla p_{\perp\sigma} - \mathbf{R})/m_\sigma n_\sigma \omega_{c\sigma} + \{(v_{t||\sigma}^2 - v_{t\perp\sigma}^2 + u_{||\sigma}^2)/\omega_{c\sigma}\}\mathbf{b}\times\boldsymbol{\kappa}$$

where $\beta = B/B$ is a unit vector, $\boldsymbol{\kappa} = (\mathbf{b}\cdot\nabla)\mathbf{b}$ is the curvature vector, $\mathbf{v}_E \sim (1+0.25\rho_s^2\nabla^2)\mathbf{E}\times\mathbf{b}/B \sim \mathbf{E}\times\mathbf{b}/B$ is the electric drift velocity including a finite gyro-radius correction, $v_{t||\sigma} = (T_{||\sigma}/m_\sigma)^{1/2}$ and $v_{t\perp\sigma} = (T_{\perp\sigma}/m_\sigma)^{1/2}$ are thermal speeds, $p_\sigma = nT_\sigma$ is the static pressure, $w_{c\sigma} = e_\sigma B/m_\sigma$ is the gyro-frequency, $\rho_\sigma = v_{t\perp\sigma}/\omega c_\sigma \sim vt_\sigma/\omega_{c\sigma}$ the thermal gyro-radius, and e_σ is the charge (-e for electrons, +Ze for ions); the parallel drift, related to mirror forces, is usually small in tokamaks and can be

neglected. The two terms in the energy flux (3.1) represent convective and conductive components, such that the latter term may be properly termed the drift related heat flux with $\chi_{\wedge\sigma} = 2.5 v_{t\sigma}\rho_\sigma$ the diamagnetic heat diffusivity [Braginskii65]. Dominant contributions to the poloidal (strictly speaking $\wedge$) components of (3.1) arise due to **E×B** and diamagnetic drifts, related to radial pressure and temperature gradients. We write these explicitly as,

$$q_{\sigma\wedge}{}^{E} \sim 2.5 p_\sigma E_\perp/B, \quad q_{\sigma\wedge}{}^{\nabla p} \sim 2.5(T_\sigma/e_\sigma B)\nabla_\perp p_{\perp\sigma}, \quad q_{\sigma\wedge}{}^{\nabla T} \sim 2.5(p_\sigma/e_\sigma B)\nabla_\perp T_\sigma \qquad (3.2)$$

Basic vector calculus suffices to show that diamagnetic heat fluxes are very nearly divergence free inside the plasma, $\nabla\cdot\mathbf{q}_\sigma{}^{\nabla p} \sim \nabla\cdot\mathbf{q}_\sigma{}^{\nabla T} \sim 0$. As such, they do not affect the energy dynamics of the plasma, which is determined by terms involving $\nabla\cdot\mathbf{q}_\sigma$, and can be neglected in most numerical simulations. This is not to say that these fluxes are fictitious; nor does it imply that they deposit no energy on the divertor targets. It can be shown that the latter does in fact apply to $\mathbf{q}_\sigma{}^{\nabla p}$, which forms a closed circuit inside the plasma due to the || pressure gradient in the magnetic pre-sheath [Stangeby00, Chankin01]. However, the same argument does not hold for $\mathbf{q}_\sigma{}^{\nabla T}$, especially $q_i{}^{\nabla T}$, since $\nabla_{||} T_i \sim 0$ at the entrance to the pre-sheath, which follows from the sheath energy transmission coefficient $\gamma_i \sim 2 - 2.5$ [Stangeby00]. Since typically $T_i/T_e \sim 2$ in the SOL, this implies a net energy deposition on the outer target in fwd-B due to both the **E×B** and conductive diamagnetic drifts. This point is illustrated in Fig.10, which shows the poloidal components of the three energy fluxes (3.2) in the forward field direction; all single arrows change sign if the field direction is reversed. In contrast, the double arrows, indicating the direction of gradients, remain unchanged in field reversal. It is worth noting the strong shear in the poloidal **E×B** velocity, which is linked to the turbulence reduction and edge transport barrier formation [Connor99, Connor00]; we will return to this important point in Section 5.

To first order, we can estimate the radial electric field as $E_\perp \sim 3\nabla_\perp T_e$, which should be evaluated at the outer target. Writing the poloidal component of the parallel energy flux as $q_{\theta\sigma} = (B_\theta/B)q_{||\sigma}$ with $q_{||\sigma} \sim p_\sigma L_{||}/\tau_{||\sigma}$ and $\tau_{||i} \sim L_{||}/c_s$, $\tau_{||e} \sim L_{||}{}^2/\chi_{||e}$, we find

$$\begin{aligned} q_{\theta i}{}^{E}/q_{\theta i} &\sim 3\nabla_\perp T_e/c_s B_\theta \sim 3\rho_{\theta s}/\lambda_{Te}, & q_{\theta e}{}^{E}/q_{\theta e} &\propto \nu^*_e \rho_{\theta s}/\lambda T_e \\ q_{\theta i}{}^{\nabla T}/q_{\theta i} &\sim \nabla_\perp T_i/c_s e_i B_\theta \sim \rho_{\theta s}/\lambda_{Ti}, & q_{\theta e}{}^{\nabla T}/q_{\theta e} &\propto \nu^*_e \rho_{\theta s}/\lambda T_e \end{aligned} \qquad (3.3)$$

where $\rho_{\theta s}$ is the poloidal gyro-radius evaluated at the sound speed. Hence the ratio of the poloidal components of the drift and parallel heat fluxes can be estimated as the gyro-radius normalised by the temperature gradient length, $\lambda_{T\sigma} \equiv |\nabla_\perp T_\sigma/T_\sigma|^{-1}$. Since $\lambda_q \sim (3 - 5)\rho_i \sim (1 - 1.5)\rho_{\theta i}$ in high power H-modes on JET, with typical $\lambda_{T\sigma} \sim (2 - 3)\lambda_q$, we can expect $\rho_{\theta i}/\lambda_{Ti} \sim O(1)$ and thus a significant contribution from drift effects for low ν^*_i. Using the experimental scaling of λ_q (2.1(a)) as a rough guide for the $\lambda_{T\sigma}$ scaling, we find that the field dependence cancels, leaving a positive, roughly linear, power scaling,

$$\{q_{\sigma\wedge}{}^{E}, q_{\sigma\wedge}{}^{\nabla T}\}/q_{\wedge\sigma} \propto T_{\sigma,\,u}{}^{0.5} P_{SOL}{}^{0.5} n_{e,\,u}{}^{-0.2} \qquad (3.4)$$

in rough agreement with experiment [Pitts05]. This result offers clear evidence for the guiding centre drift origin of the (**B**×∇B dependent) poloidal energy fluxes in the SOL, required to explain the observed out-in divertor power asymmetries.

The above conclusions have been largely confirmed by numerical simulations of matched fwd-B and rev-B discharges using the EDGE2D fluid transport code in which classical drift effects have been included and radial transport coefficients were varied poloidally to increase the energy outflux on the low field side [Kirnev05, Fundamenski05]. The largely divergence free, diamagnetic drifts ($\nabla\cdot\mathbf{q}_\sigma{}^{\nabla p} \sim \nabla\cdot\mathbf{q}_\sigma{}^{\nabla T} \sim 0$) have been excluded from EDGE2D for numerical reasons. The simulations are able to reproduce the observed in-out power asymmetries with reasonable accuracy, eg. see Fig.4 of [Fundamenski05], suggesting that the $\wedge$ component of the **E×B** drift, that is $(E_\perp/B)\mathbf{e}_\wedge$, plays a dominant role in the poloidal energy flux in the SOL.

3.3 ASCOT SIMULATIONS OF ION ORBIT LOSS

The strong sensitivity of ion orbit loss to field reversal was already illustrated in Fig.2. In this sub-section we present a more detailed analysis, also performed using the ASCOT code descirbed in Section 2.2. The pedestal and SOL plasma profiles were chosen to match the extensively modelled fwd-B Pulse No: 50401 (2.5MA/2.4T, 12MW NBI), which has the same field, current and heating power as the 50379/59691 forward/reversed pair. The pedestal width of 15mm-omp was assumed in the modelling, which is equivalent to $2.5\rho_{\theta i}$ at the outer mid-plane, with $T_{i,\,ped} \sim 1.1$keV and $T_{i,\,sep} \sim 400$eV. In the first stage, a series of trace simulations were performed to test the effects of:

- poloidal launch location (outer mid-plane, inner mid-plane or uniform; $\theta_0 = 0, \pi, 0 - 2\pi$)
- radial launch location (whole pedestal region, $\rho_0 = 0.95 - 1$, or separatrix, $\rho_0 = 1$)
- anomalous diffusion ($D_\perp{}^{an} = 0 - 1\ m^2/s$)
- radial electric field in the SOL ($E_\perp{}^{SOL} = 0 - 75$kV/m)
- toroidal field ripple (the relative change of the toroidal field on JET with the standard 24TF coils is $\sim 10^{-3}$ near the outer mid-plane; $B_{rip}/B = 0 - 10^{-3}$).

The results are gathered in Table 2, with the out-in asymmetry of deposited particle fluxes, Γ_o/Γ_i, powers, P_o/P_i, and peak heat loads, q_o/q_i tabulated for both field directions. As expected, all three quantities, especially q_o/q_i, are strongly affected by field reversal, irrespective of the parametric scans described above. The only exception is the case with a very large value of radial diffusivity, $D_\perp{}^{an} \sim 1 m^2 s^{-1}$, in addition to a significant value of the electric field in the SOL, $E_\perp{}^{SOL} \sim 50$kV/m. However, even these somewhat unrealistic assumptions are insufficient to account for both fwd-B and rev-B data, which provides a strong indication that direct ion orbit loss in not dominant in these experiments.

The results of Table 2 merit a few remarks. First, we note that P_o/P_i is not sensitive to either i-i or i-n collisions. Second, it is clear that it increases with $E_\perp{}^{SOL}$ for fwd-B and decreases with

$E_\perp^{SOL}$ for rev-B, consistent with the direction of the **E×B** drift. Third, as expected from Fig.2, the asymmetry is a strong function of the poloidal launch location, with $P_o/P_i >> 1$ for outboard launch and $P_o/P_i << 1$ for inboard launch. Fourth, in the case of pure outboard launch, P_o/P_i is only weakly sensitive to $E_\perp^{SOL}$. Finally, we consider the effect of additional radial diffusivity mechanisms, i.e. $D_\perp^{an}$ and B_{rip},

- $D_\perp^{an} = 1m^2s^{-1}$, $E_\perp^{SOL} = 0$: $P_o/P_i \sim 2$ in agreement with purely geometrical predictions,
- $D_\perp^{an} = 1m^2s^{-1}$, $E_\perp^{SOL} = 75kV/m$: $P_o/P_i \sim 5$ for fwd-B and ~ 1.5 for rev-B indicating strong influence of the **E×B** drift; this result is notable in that $(P_o/P_i)_{fwd\text{-}B} > (P_o/P_i)_{rev\text{-}B}$ as observed in experiment, suggesting that additional radial diffusion is needed to explain the observed asymmetry.
- The toroidal field ripple at the level of $B_{rip}/B \sim 10^{-3}$ has little effect, irrespective of the value of $E_\perp^{SOL}$.

In the second stage, self-consistent simulations were performed with three values of E $E_\perp^{SOL}$: 0, 45 and 75kV/m; this range of $E_\perp^{SOL}$ is motivated by earlier studies, which indicated that $E_\perp^{SOL} \sim$ 50kV/m is required to match the narrow profiles on the outer target observed at JET [Fundmanenski03]. The resulting heat load profiles on both targets are shown in Fig.11 (or Fig.5 of [Fundamenski05]), including the peak heat loads q_{peak} and the power widths λ_q. We first note that only the $E_\perp^{SOL} = 75kV/m$ case yields ion peak powers in excess of $5MW/m^2$ as measured for this shot. It is therefore necessary to consider the effect of field reversal on the simulated power deposition profiles, primarily for the 45 and 75kV/m cases. This effect is quite dramatic, with the outer profiles drastically broadened by a factor of 5 – 6 and peak values reduced by comparable amounts. The asymmetry q_o/q_i changes from 3.3 – 8.7 for fwd-B to 1.1 – 0.54 for rev-B, for the 45 and 75kV/m cases. This behaviour is in sharp contrast to experiment where peak values change at most by a factor of two, and little broadening of λ_q is observed, Fig.8 and Fig.9. We are thus led to conclude that direct orbit loss is not responsible for the observed target profiles. Instead, (neo-)classical ion transport, including the effects of collisional ion orbit loss, discussed in §2, is the most likely explanation for the observed data. As has been noted in §2, this does not rule out ion orbit loss as such, but only collisionless losses of hot ions from the top of the pedestal. The simulations further suggest that ion-ion collisions in the SOL are required to modify the loss ion orbit and produce profiles and asymmetries more in line with the experiment. This results in Pfirsch-Schlutter-like radial diffusion of heat with an intermediate dependence on q_{95}, which we defined as (neo-)classical.

To summarise the section, we note that the field reversal experiments lead to three main conclusions:

- **B×**∇B direction affects the polodial power flow in the SOL and hence the power flow into the divertor
- the direction, magnitude and scaling of this poloidal power flow can be explained by classical drift-related heat fluxes (mostly **E×B**, with a possible contribution from **B×**∇T_σ); this conclusion is supported by numerical simulations using the EDGE2D code.

- radial transport is largely independent of the **B**×∇B direction; in terms of determining the dominant power exhaust mechanism in the SOL, this key finding weighs heavily in favour of collisional transport, namely (neo-)classical ion conduction, which is independent of **B**×∇B direction, and rules out direct ion orbit loss which exhibits a strong **B**×∇B dependence. This conclusion is confirmed by detailed ASCOT simulations of direct ion orbit loss under realistic JET conditions, which cannot explain the experimental variation of deposited profiles with **B**×∇B.

4. INTERPRETATION OF ELECTRON PROFILE MEASUREMENTS IN THE SOL

Whereas the results reported in Section 2 and 3 are based on total (ion + electron) divertor power profiles (characterised by λ_q), most previous studies dedicated to characterising SOL plasma profiles have relied on Langmuir probe measured electron power or pressure profiles (characterised by λ_q^e), with the ultimate aim of identifying the mechanisms governing radial energy transport in the SOL. These studies, which were necessarily restricted to the electron channel, may be divided into two categories: the first relied on λ_q^e measured in the upstream SOL and pedestal regions, while the second were based on λ_q^e corresponding to divertor target n_e and T_e profiles. We will refer to these as the upstream and downstream approaches, respectively. In this section, we consider these in turn, comparing the results in each category with available theories of radial heat diffusivities.

The upstream approach was used to analyse pressure electron profiles from two large machines: AUG [Kim01] and JET [Kallenbach04]. We begin with the AUG study, which was by far more extensive. It was based on the 2-D fluid transport code SOLPS5, which was used to match the upstream profiles of both L and H-mode discharges with $n/n_{GW} \sim 0.35$ - 0.8 and $\nu_e^* \sim$ 4-50. The following expressions were obtained in terms of engineering, plasma and dimensionless variables [Kim02],

$$\begin{aligned} \chi_\perp &= 0.23\times B_\phi^{-2.31\pm0.65} I_p^{-1.1\pm0.29} P_{SOL}^{1.14\pm0.12} \langle n_e \rangle^{0.58\pm0.23} \\ \chi_\perp &\propto B_\phi^{-1.83\pm1.04} B_\theta^{-0.41\pm0.47} T_e^{1.12\pm0.26} n_e^{1.11\pm0.26} n_0^{0.62\pm0.24} \\ \chi_\perp &= 1.1\times10^5\times\chi_B\times\beta^{1.45\pm0.26} \nu_e^{*0.68\pm0.12} S^{-2.2\pm1.64} (n_0/n_e)^{0.51\pm0.24} \end{aligned} \quad (4.1)$$

where $\chi_\perp$ is the SOL heat diffusivity in m^2s^{-1}, I_p in MA, P_{SOL} in MW, $\langle n_e \rangle$ and n_0 (the neutral density) in 10^{19} m^{-3}, S is the magnetic shear, and $\chi_B \propto T_e/B$ the Bohm diffusivity. Although, the authors do not compare their results with all available theories, this comparison may be obtained based on the set of theories of §2. Since the diffusivities $\chi_\perp$ themselves are extracted, these may be compared directly with theoretical predictions. The error between the theoretical and experimental scalings with respect to $\{n_e, T_e, q_{95}, B_\phi\}$ is shown as a bar chart in Fig.12, similar to Fig.6, where each bar represents a single theory and different shades represent contributions from different exponents in the scaling. The root-mean-square error is ~ 0.6 for theories {**K2, G2, F, L1, K1, G1, B1, B2**}, and ~ 0.8 for {**A1, A3, N**}, and rises rapidly for the rest; here **G2** denotes endplate MHD

interchange, **G1** MHD interchange, **F** drift wave, **L** sheath modes, **K1** and **K2** the drift Alfven modes at low and high collisionality, and **B1** and **B2** endplate MHD interchange with λ_p and λ_n. The study of fuelled (f_{GW} ~ 0.7 - 1), type-I ELMy H-modes on JET (ν_e^* ~ 8 - 40) using the EDGE2D fluid transport code finds [Kallenbach04],

$$\chi_\perp \propto B_\phi^{-1.3\pm0.5} P_{heat}^{0.9\pm0.5} \langle ne \rangle^{0.5\pm0.5} \tag{4.2}$$

roughly consistent with the AUG result, despite a weaker B_ϕ scaling. Broadly speaking both studies suggest that upstream pressure profiles are governed by electrostatic turbulence, driven by MHD interchange (**B1, B2, G1, G2**), drift and/or drift-Alfven (**F, K1, H2**) and sheath resitive (**L1**) modes.

The downstream approach was used to examine divertor Langmuir probe profiles from three tokamaks: COMPASS-D (ohmic, L-mode, ν_e^*~0.2-3), Alcator C-Mod (ohmic, ν_e^*~20-370), and JET (ohmic, L, H-mode, ν_e^*~10-100) [Connor99, Counsell99]. In all cases, a simplified SOL model was used to relate LP-measured target λ_q^e to the heat diffusivity $\chi_\perp$, following the method outlined in Section 2. Comparison with theory focussed on scaling with respect to $\{n_e, P_{SOL}, q_{95}, B_\phi\}$ since variation of the plasma species was in general unavailable. For $\nu_e^* > 10$, five theories emerge as noticeably better than the rest, error < 0.2: {**D, O, J, J3, M, Q**} for C-Mod, and {**D, M, O, J, J3**} for JET, where **D** denotes collisionless MHD interchange near $\beta_{critical}$, **O** the collisionless skin depth, **J** drift with collisionless skin depth, **M** charge-exchange and **Q** the null model, $\chi_\perp$ = constant. The fact that both JET and C-Mod suggest the same subset of theories, increases the credibility of these results. Once again, the results point to MHD interchange and drift-Alfven instabilities, but suggest divertor target electron power profiles may also be influenced by charge-exchange and skin depth effects.

Let us summarise the electron energy transport results. As expected from (2.4), where we saw that $\lambda_q \sim 20\times\lambda_q^{A3}$ and hence $\chi_\perp \sim O(10^3)\times\chi_\perp^{A3}$, comparison of scaling results indicates that the observed electron pressure profiles are indeed governed by turbulent convection. Among the leading candidates for the turbulent drive, MHD interchange instabilities are expected to be strongly active in the SOL region, while the drift-Alfven instabilities are expected to predominate in the pedestal region (and might affect the near-SOL by turbulence spreading in to the SOL and subsequent damping).

5. TURBULENT VS. COLLISIONAL ENERGY TRANSPORT IN THE NEAR-SOL

The conclusions reached in Section 4, are entirely consistent with current understanding of turbulent transport in the SOL [Itoh99, Scott01]. The existence of substantial fluctuations of density and electric potential in the scrape-off layer is a well established experimental fact [Huggill00, Stangeby00]. Relative fluctuations are much larger in the SOL than in the core plasma (> 50% in SOL vs. than < 10% in the core), and are generally consistent with the experimental finding that fluctuation levels increase with minor radius. In addition, they often persist even under H-mode

conditions, although this is only widely established for the far-SOL, since diagnosing the near-SOL region in high power discharges poses substantial diagnostic challenges [Erents00]. Finally, the overall level of fluctuations is highly intermittent, as observed in radially propagating filaments or blobs; the level of intermittency typically increases with radius and is larger in the far-SOL.

The origin of SOL turbulence can be traced to the absence of either ergodic or closed flux surfaces outside of the separatrix. The formation of the plasma sheath on open field lines at the divertor targets gives rise to the so-called sheath resistivity. Consequently, the presence of the sheath impedes parallel return currents needed to maintain flux tube charge neutrality in the presence of the magnetic and thermodynamic gradients, and the ensuing charge-dependent drifts. Insufficient return current leads to a local charge imbalance, which in turn produces radial **E×B** drift of individual plasma filaments. Each open flux tube in the SOL is thus subject to a destabilising outward drift, which tends to be stronger in regions of unfavourable magnetic curvature. Somewhat surprisingly, this obvious fact is often obscured, if not misrepresented, in the topical literature. For example, it is often suggested that SOL turbulence originates in the pedestal region, which could be misconstrued to mean that the SOL plays only a passive, perhaps even a stabilising role in the propagation of pedestal induced disturbances. The latter is clearly not true. While a perturbation originating in the pedestal region (eg. drift-Alfven driven turbulence) can propagate into and dissipate in the SOL, the SOL plasma itself can and does produce a range of turbulent activity (eg. MHD interchange instabilities) irrespective of the pedestal dynamics. To draw an analogy with hydrodynamics, the SOL is subject to both pressure gradient driven (Rayleigh-Taylor) and velocity gradient driven (Kelvin-Helmholtz) instabilities.

In short, the bad curvature region of the SOL is not in equilibrium in the sense of ideal MHD, i.e. the balance of thermal and Lorentz forces, $\mathbf{j}\times\mathbf{B} = \nabla_p$, is impeded both by the finite parallel resistivity of the relatively cold (<100eV) SOL plasma and the resistivity of both the inner and outer target Langmuir sheaths. The SOL plasma is thus inherently unstable to a range of MHD modes, first among which are interchange instabilities driven by magnetic curvature and radial pressure gradients [Hazeltine92]. As a result, we expect to find quite intense turbulent activity in the SOL, as is indeed observed in experiment. Since parallel losses to the divertor targets rapidly remove the thermal energy from the SOL plasma, we also expect SOL turbulence to be much more dissipative than turbulence in regions of closed field lines [Scott01]; here the term dissipative signifies decay of kinetic energy associated with turbulent eddies. The large radial electric fields in the near-SOL form a strong poloidal velocity shear (zonal flow) in a relatively narrow region of order λ_q, ripping apart the larger eddies due to vorticity effects and self-regulating the level of turbulence [Itoh99, Diamond05]. Finally, the SOL plasma being strongly magnetised, turbulent plasma eddies are highly elongated along the magnetic field, with the resulting eddy motions, confined to the $\perp$-$\wedge$ plane. In short, SOL turbulence should to first order evolve in two dimensions, with the term eddy signifying an extended plasma filament. We adopt the term filament, which is more suggestive of the 2-D nature of SOL turbulence, rather than such terms as blob [Krasheninnikov01], avaloid [Antar01],

burst [Hidalgo03], plasmoid [Fundamenski04a] or front [Ghendrih03] which may be found in recent SOL literature. It is the radial motion of these filaments, averaged over all scales, which results in the enhanced convective transport of energy [Biskamp03, Taylor97, Naulin02, Antar01, Rudakov05]. Finally, the formation of large structures in the $\perp$-$\wedge$ plane (usually referred to as blobs) follows naturally due to an inverse energy cascade in 2-D turbulence [Biskamp03]. All of these characteristics (filamentation, intermittency, zonal flow, dissipation, etc.) have been observed in numerical simulations of SOL turbulence, with different levels of sophistication [Beyer99, Xu99, Naulin02, Garcia04, Graves05]. The theoretical framework of SOL turbulence thus appears to be well established and capable of explaining the observed phenomenology.

We may therefore ask how the conclusions reached in Sections 2 and 3, namely that net energy transport in the near-SOL is dominated by collisional diffusion, can be reconciled with the conclusion of Section 4 that electron energy transport is dominated by turbulent convection. In other words, is there an inconsistency between these two conclusions, i.e. laminar transport for ion energy and turbulent transport for electron energy channels? In this section we show that this apparent inconsistency is purely illusory, and that the two mechanisms are in fact entirely compatible.

An initial attempt to resolve this apparent contradiction was offered in Section 2, where it was shown that in order to match the observed target profiles - typically $\lambda_q/\rho_i \sim 3\times\lambda_q/\rho_{\theta i} \sim O(5)$ while $\lambda_q/\rho_e \sim O(100)$ - one must assume significant levels of turbulence in the near-SOL, even in the presence of an H-mode barrier! With this assumption, turbulent convection entirely determines the radial transport of electron energy in the SOL, $\chi_{\perp e}/\chi_\perp^{A3} \sim O(10^3)$. The same argument can be repeated for radial particle and momentum transport, which depend on electron-ion collisions. However, as was also found in Section 2, turbulent convection has a far smaller effect on the radial transport of ion energy on account of the larger gyro-radius and hence the ion collisional heat diffusivity, which is determined solely by ion-ion collisions, $\chi_{\perp i}/\chi_\perp^{A2} \sim O(1)$. In other words, both turbulent and collisional transport processes are active in the near-SOL, although the latter are evidently dominant for the radial transport of ion energy.

In the absence of global SOL turbulence simulations of sufficient resolution to capture both turbulent and collisional effects, we must necessarily resort to approximate analysis. One possible route often employed in turbulence theory, is to adopt the phenomenology of the eddy cascade and consider the evolution of some quantity of interest, in our case of the thermal energy, for a turbulent plasma filament of arbitrary size; this approximation reduces the problem from one of differential to that of algebraic analysis. To study the interplay of turbulent and collisional transport, we can focus on the radial length scale at which the two mechanisms are comparable, which in turbulence theory is known as the dissipative scale, l_σ. The concept of the dissipative scale is briefly introduced in Appendix A. This scale is especially appropriate to SOL turbulence which, due to parallel losses to the divertor targets, is highly dissipative in nature.

The analysis in the remainder of the section is systematically developed as follows: The energy balance for a magnetised plasma filament is introduced in Section 5.1, including the ordering of the

heat fluxes and loss times in the ($\|$, $\wedge$, $\perp$) basis. Filament energy losses in each of these directions are then discussed in turn in Sections 5.2 – 5.4. Finally, the dissipative scale is derived in Section 5.5 by equating the loss times obtained in Sections 5.2 and 5.3, and applied to the interpretation of JET experimental results.

5.1 ENERGY EVOLUTION IN THE FILAMENT FRAME OF REFERENCE

Consider a plasma filament consisting of ions and electrons of average density, $n_\sigma \sim n$ temperature, T_σ and velocity, υ with components, u_μ in the rest (lab) frame, where $\sigma \in \{i,e\}$ is a species index and $\mu \in \{\|, \wedge, \perp\}$ is a directional index, Fig.13; all filament quantities denote volumetric averages. We define the size of the filament by three lengths, $\delta_\|$, $\delta_\wedge$ and $\delta_\perp$. Quasi-neutrality and weak parallel currents are assumed, such that $n_e \sim n_i \sim n$, $u_{\|i} \sim u_{\|e} \sim u_\|$. The ratio $\vartheta \equiv T_i/T_e$ is treated as a free parameter. The parallel plasma velocity $u_\|$ is assumed to be subsonic with respect to the plasma sound speed $c_s = [(ZT_e+T_i)/m_i]^{1/2} = \xi v_{ti}$ where Z is the ion charge, $v_{ti} = (T_i/m_i)^{1/2}$ is the ion thermal velocity and $\xi \equiv (1+Z/\vartheta)^{1/2}$; it is written as $u_\| = M\xi v_{ti}$ with the Mach number $M = u_\|/c_s$ treated as a free parameter.

We are interested in the evolution of the filament energy density $\varepsilon_\sigma \sim n(3/2\times T_\sigma + 1/2\times m_\sigma u_\|^2)$ for both plasma species. This follows from the energy conservation equation for each species which, neglecting volumetric sources and sinks, may be written in the divergence form as [Braginskii65, Huba02],

$$\begin{aligned}
\partial\varepsilon_\sigma/\partial t + \nabla_\| q_{\|\sigma} + \nabla_\perp q_{\perp\sigma} + \nabla_\wedge q_{\wedge\sigma} + (\varepsilon_\sigma - \varepsilon_{\neg\sigma})/\tau_{ie} &= 0 \qquad (5.1)\\
q_{\|\sigma} = q_\| v,_\sigma + q_{\|\chi,\sigma} &= (5/2\times T_\sigma + 1/2\times m_\sigma u_\|^2)nu_\| - n\chi_{\|\sigma}\nabla_\| T_\sigma,\\
q_{\perp\sigma} = q_\perp v,_\sigma + q_{\perp\chi,\sigma} &= (5/2\times T_\sigma + 1/2\times m_\sigma u_\|^2)nu_\perp - n\chi_{\perp\sigma}\nabla_\perp T_\sigma,\\
q_{\wedge\sigma} = q_\wedge v,_\sigma + q_{\wedge\chi,\sigma} &= (5/2\times T_\sigma + 1/2\times m_\sigma u_\|^2)nu_\wedge - n\chi_{\wedge\sigma}\mathbf{b}\times\nabla_\perp T_\sigma
\end{aligned}$$

Here $q_{\mu v,\, s}$, $q_{\mu\chi,\,\sigma}$ and qms denote respectively the $\mu\in\{\|, \wedge, \perp\}$ components of the convective, conductive and total energy fluxes of species σ, while $(\varepsilon_\sigma - \varepsilon_{\neg\sigma})/\tau_{ie}$ is the collisional ion-electron energy transfer term, with τ_{ie} the ion-electron energy equilibration time. The ratio of compressional, $1/2\times n_\sigma m_\sigma u_\|^2$ to thermal, $3/2\times p_\sigma$ energy may be written as, $m_\sigma u_\|^2/T_\sigma \sim (u_\|/v_{t\sigma})^2 \sim M^2(v_{ti}/v_{t\sigma})^2$. This ratio is negligible for electrons, and small for ions provided $M < 0.3$. Consequently, compressional terms will be neglected below (this simplifies, but does not alter the analysis), such that $\varepsilon_\sigma \sim 3/2\times p_\sigma$ and $q_{\mu v,\,\sigma} \sim 5/2\times p_\sigma u_\mu$. Classical, collisional heat diffusivities, $\chi_{\mu\sigma}$ have been derived as [Braginskii65, Huba02],

$$\begin{aligned}
\chi_{\|\sigma} &= c_{\|\sigma} v_{t\sigma}\lambda_{\sigma\sigma} = c_{\|\sigma} v_{t\sigma} 2\tau_{\sigma\sigma}, \quad \{c_{\|i} = 3.9,\ c_{\|e}=3.2\} \qquad (5.2)\\
\chi_{\wedge\sigma} &= c_{\wedge\sigma} v_{t\sigma}\lambda_{\sigma\sigma}/\omega_{c\sigma}\tau_{\sigma\sigma} = c_{\wedge\sigma} v_{t\sigma}\rho_\sigma, \quad \{c_{\wedge\sigma} = 2.5\}\\
\chi_{\perp\sigma} &= c_{\perp\sigma} vt_\sigma\lambda_{\sigma\sigma}/(\omega_{c\sigma}\tau_{\sigma\sigma})^2 = c_{\perp\sigma}\rho_\sigma^2/\tau_{\sigma\sigma}, \quad \{c_{\perp i} = 2,\ c_{\perp e}= 4.7\}
\end{aligned}$$

where $\lambda_{\sigma\sigma}$ is the mean-free-path, $\rho_\sigma \sim v_{t\sigma}/\omega_{c\sigma}$ the gyro-radius, $\omega_{c\sigma}$ the gyro-frequency and $\tau_{\sigma\sigma}$ the characteristic collision time for σ-σ Coulomb scattering [Miyamoto87],

$$\tau_{\sigma\sigma} \propto Z_\sigma^{\,4} m_\sigma^{\,1/2} T_\sigma^{\,3/2} n^{-1} \tag{5.3}$$

Two ordering hierarchies emerge: the ordering of collisional times,

$$\tau_{ie} : \tau_{ii} : \tau_{ee} : \tau_{ei} \approx Z_i^{\,-2}(m_i/m_e) : (m_i/m_e)^{1/2} Z_i^{\,-3} \vartheta^{3/2} : 1 : Z_i^{\,-1} \tag{5.4}$$

and the ordering of heat diffusivities,

$$\chi_{\perp\sigma} : \chi_{\wedge\sigma} : \chi_{\|\sigma} \sim (\omega_{\chi\sigma}\tau_{\sigma\sigma})^{-2} : (\omega_{\chi\sigma} t_{\sigma\sigma})^{-1} : 1 \tag{5.5}$$

where, for typical JET near-SOL conditions, $\omega_{ce}\tau_{ee} \sim (m_i/m_e)^{1/2}\vartheta^{-3/2}\omega_{ci}\tau_{ii} \sim O(10^4)$. The strong anisotropy of transport in the SOL is apparent from (5.5), which indicates that collisional heat diffusion is many orders of magnitude faster in the parallel direction than cross-field: $\chi_{\perp e}/\chi_{\|e} \sim O(10^{-8})$!

Analogous to Appendix A, we replace all spatial gradients by the inverse size of the filament, $\nabla_\mu \rightarrow \delta_\mu^{\,-1}$ such that equation (5.1) may be re-written in the zero dimensional form,

$$(\partial/\partial t + \tau_{\|s}^{\,-1} + \tau_{\perp\sigma}^{\,-1} + \tau_{\wedge\sigma}^{\,-1})\varepsilon_\sigma + (\varepsilon_\sigma - \varepsilon_{\neg\sigma})/\tau_{ie} = 0 \tag{5.6}$$

where $\tau_{\mu\sigma}$ are characteristic energy transport (or loss) times. The ion-electron equipartition time is much longer than the ion-ion and electron-electron collision times (5.4), $\tau_{ie} >> \tau_{ii} >> \tau_{ee}$, and will consequently be neglected. The typical time scale of parallel and collisional times for $L_\| = 30$m, $n = 10^{19}$ m^{-3} and 10eV < T_e < 1000eV are shown in Fig.1 of [Fundamenski04a], in which the hierarchy of collisional times (5.4) is clearly visible.

As sketched out in Appendix A, the derivation of the dissipative scale requires that we circumvent the non-linear advection terms by adapting the frame of reference moving with the filament in the $\perp$-$\wedge$ plane, in which the velocities $u_\perp = u_\wedge = 0$ and the convective terms $q_{\wedge v,\,\sigma} = q_{\perp v,\,\sigma} = 0$ in (5.1) vanish. Of course, the SOL radial profiles are measured in the lab frame of reference. Only radial filament motions will effect these profiles, since the diamagnetic motions merely distribute the energy within the flux surface. The effect of radial filament velocity, $u_\perp \neq 0$ on the lab frame SOL profiles is briefly considered below. The effect of diamagnetic velocity, $u_\wedge \neq 0$, including the distortion of the filament by velocity shear, $\nabla_\perp u_\wedge \neq 0$, will be addressed in §5.4.

The radial power width in the lab frame in the absence of radial energy convection, $u_\perp = 0$, was obtained as (2.3). When outward radial filament motion is included, $u_\perp > 0$, this expression must be replaced by,

$$\lambda_q \sim u_\perp \tau_{||} \{1 + (1+ 4[\chi_\perp / {u_\perp}^2 \tau_{||}])^{1/2}\}/2 \qquad (5.7)$$

which reduces to $\lambda_q \sim u_\perp \tau_{||}$ in the absence of heat diffusion ($\chi_\perp = 0$) and to $\lambda_q \sim (\chi_\perp \tau_{||})^{1/2}$ in the absence of convection ($u_\perp = 0$). The effective (ensemble average) velocity in the near-SOL can be inferred from a measured profile width as $u_\perp \sim \lambda_q/\tau_{||} \sim$ which is in the range of 10m/s for typical JET near-SOL conditions; normalised to the sound speed this gives $u_\perp/c_s \sim 10^{-4}$. Since $\lambda_q \sim O({\lambda_q}^{A1})$, cf. (2.4), this is comparable to the classical diffusion velocity ${u_\perp}^{A1} \sim {\lambda_q}^{A1}/\tau_{||v} \sim \rho_i/(\tau_{ii}\tau_{||v})^{1/2} \sim$ 10m/s or, normalised to the sound speed, ${u_\perp}^{A1}/c_s \sim (\rho_i/L_{||}){\nu^*}_i^{1/2} \sim 10^{-4}$. These values are much smaller than those typically observed in the far-SOL for intermittent filament (blob) and ELM propagation: $u_\perp \sim$ 1km/s, $u_\perp/c_s \sim 10^{-3} - 10^{-2}$ [Goncalves03, Boedo05, Fundamenski04a]; these higher values are also predicted from sheath limited models and from curvature driven turbulence codes under low collisionality conditions [Beyer99, Naulin02]. In other words, radial filament motions in the near-SOL region are relatively slow in comparison with the far-SOL and appear to be governed by diffusive motions. We are therefore justified in assuming $u_\perp \sim 0$.

Assuming further that the dominant energy loss mechanisms are parallel losses and perpendicular conduction, a rough estimate of the elongation of the filament may be obtained in (5.1),

$$\delta_\perp / \delta_{||} \sim (\chi_{\perp\sigma}/\chi_{||\sigma})^{1/2} \sim (\omega c_\sigma \tau_{\sigma\sigma})^{-1}$$

which for JET is ~ $O(10^{-4})$; not surprisingly, we find the filament to be highly elongated parallel to B, with $\delta_\perp/\delta_{||}$ comparable to $\lambda_q/L_{||}$ for the SOL as a whole [Stangeby00]; this prediction is confirmed by the observed parallel correlation lengths of SOL turbulence on JET in the range of tens of meters [Thomsen02]. The above size ordering, directly yields the ordering of conductive (heat) fluxes,

$$q_{\perp\chi,\,\sigma} : q_{\wedge\chi,\,\sigma} : q_{||\chi,\,\sigma} \sim (\omega_{c\sigma}\tau_{\sigma\sigma})^{-1} : O(1) : \ 1 \qquad (5.8)$$

and the energy loss times,

$$\tau_{\perp\sigma} : \tau_{\wedge\sigma} : \tau_{||\sigma} \sim O(1) : O(1) : \ 1 \qquad (5.9)$$

which are seen to be comparable. To derived the dissipative scale, it is therefore necessary to examine the filament energy losses in all three directions, which is done in the next three sub-sections.

5.2 ENERGY DISSIPATION BY PARALLEL LOSSES

The parallel energy loss time in (5.6) may be estimated by applying $\nabla_{||} \rightarrow {\delta_{||}}^{-1}$ to (5.1),

$$\tau_{||\sigma} \sim 3/5 \times ({\tau_{v||}}^{-1} + {\tau_{\chi||\sigma}}^{-1})^{-1} \qquad (5.10)$$
$$\tau_{v||} \sim \delta_{||}/u_{||} \sim \delta_{||}/M_\xi v_{ti}, \qquad \tau_{\chi||\sigma} \sim 5/2 \times {\delta_{||}}^2/\chi_{||}\sigma$$

where $\tau_{v\|}$ and $\tau_{\chi\|\sigma}$ are the convective and conductive energy transport times for the filament [Fundamenski04a]. The first accurate derivation of $\chi_{\|\sigma}$ as stated in (5.2) was performed by Spitzer and Harm [Spitzer53], hence $\chi_{\|\sigma}^{SH} = c_{\|s} v_{t\sigma}^2 \tau_{\sigma\sigma}$. As expected, the small electron inertia results in more efficient electron heat conduction, as is evident from the ratio of ion and electron parallel heat dissusivities,

$$\chi_{\|i}^{SH} / \chi_{\|e}^{SH} \approx 1.2 \times (m_i/m_e)^{-1/2} Z_i^{-3} \vartheta^{5/2} \sim O(10^{-1}) \tag{5.11}$$

Implicit in the above derivation was the assumption of short $\lambda_{\sigma\sigma}$ as compared to both the size of the system $L_{\|}$ and the parallel gradient scale length, in this case $\delta_{\|}$. This is compactly stated as $\nu^*_{\sigma} >> 1$ in terms of the filament collisionality, $\nu^*_{\sigma} \equiv \delta_{\|}/\lambda_{\sigma\sigma} \propto \delta_{\|} n/T_{\sigma}^2$ which is mass independent. Hence,

$$\nu^*_i / \nu^*_e = (T_i/T_e)^{-2} = \vartheta^{-2} \tag{5.12}$$

which yields $0.1 < \nu^*_i / \nu^*_e < 1$ for typical SOL conditions ($1 < \vartheta < 3$), i.e. the ions are less collisional by virtue of being hotter. As the collisionality is reduced below unity ($\nu^*_{\sigma} < 1$), we expect the conductive energy fluxes to saturate at some fraction of the half-Maxwellian free streaming (FS) flux [Chapman58], $q_{\|\chi,\sigma}^{FS} \sim 0.8 \times n T_{\sigma} v_{t\sigma}$. We thus write the flux limited value of the conductive energy flux as $q_{\|\chi,\sigma}^{FL} \sim \alpha_{\sigma} n T_{\sigma} v_{t\sigma}$, where α_{σ} is some constant of order unity. There are at present no universally valid expressions for α_{σ}, which are known to depend both on plasma parameters and local gradient lengths. Below, we adopt $\alpha_i \sim 1$ and $\alpha_e \sim 0.2$ as nominative values suggested by kinetic simulations [Cohen94]; although it has been suggested that larger values, $\alpha_i \sim 3$ and $\alpha_e \sim 0.45$, may be more appropriate for transient response (the results of the analysis are only weakly sensitive to the particular choice of α_i and α_e within this range of values).

A transitional estimate of $\chi_{\|\sigma}$ which reduces to the appropriate expressions in the low and high collisionality limit is offered by the harmonic average form [Stangeby00],

$$\chi_{\|\sigma} = \chi_{\|\sigma}^{SH} / (1 + |q_{\|\chi,\sigma}^{SH} / q_{\|\chi,\sigma}^{FL}|) \sim c_{\|\sigma} v_{t\sigma}^2 \tau_{\sigma\sigma} / (1 + \nu^{*c}_{\sigma} / \nu^*_{\sigma}) \tag{5.13}$$

where $\nu^{*c}_{\sigma} = c_{\|\sigma} / \alpha_{\sigma}$ is the critical collisionality at which kinetic corrections to the Spitzer-Harm expressions become important. Based on $c_{\|\sigma}$ and α_{σ} given above we find $\nu^{*c}_i \sim 4$ and $\nu^{*c}_e \sim 16$. The kinetic corrections to parallel heat conduction as measured by the normalised collisionality $\nu^*_{\sigma} / \nu^{*c}_{\sigma}$ are thus comparable for ions and electrons under typical SOL conditions ($T_i/T_e = \vartheta = 2$) irrespective of the level of collisionality.

The ratio of conductive and convective times may be obtained by combining (5.2), (5.3), (5.10) and (5.13),

$$\tau_{\chi\|\sigma} / \tau_{v\|} \sim 5/2 \times (M\xi / c_{\|\sigma}) \times (v_{ti}/v_{t\sigma}) \times (\nu^*_{\sigma} + \nu^{*c}_{\sigma}) \tag{5.14}$$

which is a linear function of both M and ν^*_σ. The ratio vanishes as M Æ 0 (conduction dominates), but approaches a finite value as $\nu^*_\sigma \to 0$ (conduction dominates only below some critical Mach number M^c_σ). Conversely $\tau_{\chi\|\sigma}/\tau_{v\|} \to \infty$ as either M or $\nu^*_\sigma \to \infty$ (convection dominant for sufficiently large M or ν^*_σ). The transition condition may be found as a surface in the M, ϑ and ν^*_σ space (assuming Z = 1 for simplicity). Writing (5.14) separately for ions and electrons,

$$\tau_{\chi\|i}/\tau_{v\|} \sim 5/2\times(M\xi/3.9)\times(\nu^*_i + 4) \qquad (5.15)$$
$$\tau_{\chi\|e}/\tau_{v\|} \sim 5/2\times(M\xi\vartheta^{1/2}/3.2)\times(m_e/m_i)^{1/2}\times(\nu^*_e + 16)$$

the critical Mach numbers M^c_σ may be found be setting $\tau_{\chi\|\sigma}/\tau_{v\|}$ to unity. The solution is shown graphically in Fig.14, where M^c_σ is plotted as a function of ν^*_σ for different values of ϑ. In the range ($1 < \vartheta < 10$; $1 < \nu^*_\sigma < 100$) we find $0.01 < M^c_i < 0.3$ and $0.3 < M^c_e < 3$. As expected, convection is found to be always more important for ion energy transport, $M^c_i << M^c_e$; for subsonic flows parallel convection is much smaller than parallel electron conduction.

5.3 ENERGY DISSIPATION BY PERPENDICULAR LOSSES

We next consider the radial energy loss time associated with classical heat conduction, $\chi_{\perp\sigma}$ and mass diffusion, $D_\perp$ obtained from (5.1) by applying $\nabla_\perp \to \delta_\perp^{-1}$,

$$\tau_{\perp\sigma} \sim 3/5\times(\tau_{v\perp}^{-1} + \tau_{\chi\perp\sigma}^{-1})^{-1} \qquad (5.16)$$
$$\tau_{v\perp} \sim \delta_\perp/v_\perp^D, \qquad \tau_{\chi\perp\sigma} \sim 5/2\times\delta_\perp^2/\chi_{\perp\sigma}$$

where $\chi_{\perp\sigma}$ is given by (5.2) and $v_\perp^D \sim D_\perp(\nabla_\perp n)/n$; the larger ion gyro-radius, $\rho_i/\rho_e = (\vartheta m_i/m_e)^{1/2} >> 1$, gives rise to much faster $\perp$ ion conduction,

$$\chi_{\perp i} / \chi_{\perp e} \approx 0.43(m_i/m_e)^{1/2}\vartheta^{-1/2} > O(10) \qquad (5.17)$$

Since radial mass diffusion occurs via electron-ion collisions, it follows that [Miyamoto87],

$$D_\perp \sim \rho_e^2/\tau_{ei} \sim \rho_e^2/\tau_{ee} \sim \chi_{\perp e} / 4.66 \qquad (5.18)$$
$$\chi_{\perp i} : \chi_{\perp e} : D_\perp \sim 2.33(m_i/m_e)^{1/2} : 4.66 : 1$$

The energy flux carried by classical radial diffusion, $5/2\times nT_\sigma v_\perp^D \sim 5/2\times T_\sigma(D_\perp\nabla_\perp n)$ is thus small compared to both electron and ion conductive fluxes, or $\tau_{v\perp} > \tau_{\chi\perp e} >> \tau_{\chi\perp i}$ and can be neglected in (5.16), such that $\tau_{\perp\sigma} \sim 3/2\times\delta_\perp^2/\chi_{\perp\sigma}$.

5.4 ENERGY DISSIPATION BY DIAMAGNETIC LOSSES, INCLUDING VELOCITY SHEAR

According to (5.8), the parallel and radial heat fluxes are comparable. This is confirmed

experimentally in the strong effect of field reversal on the net poloidal energy flux, q_θ which is composed of the drift related energy flux, $q_\wedge$ and the parallel energy flux, $q_{||}$; since only the former is sensitive to the B×∇B direction and is therefore responsible for the observed change in q_θ we infer that the poloidal projections of $q_\wedge$ and $q_{||}$ are comparable, see §3. In the context of the filament energy balance, we therefore the expect energy loss time in the $\wedge$ direction, $\tau_{\wedge\sigma} \sim \delta_\wedge^2/\chi_{\wedge\sigma}$ where $\chi_{\wedge\sigma} = 2.5 v_{t\sigma}\rho_\sigma$ is the diamagnetic heat diffusivity, to be comparable to the parallel loss time (5.10); this result has already been anticipated in (5.18). Since, we are primarily interested in energy transport normal to the flux surface, we are justified in neglecting the $\wedge$ direction in the following analysis, by setting $u_\wedge = q_\wedge = 0$, thereby reducing the problem to two dimensions (||, $\perp$). This approach is commonly adapted in SOL modelling where the || and $\wedge$ directions are combined, and treated by a single, poloidal co-ordinate θ; the (θ, r) co-ordinates are ubiquitous in both fluid [Ronglien99, Chankin01, Bonnin03] and turbulence [Xu98, Beyer99, Naulin02, Nashimura04] codes. The essential point for the present analysis, is that all three co-ordinates (||, $\wedge$, θ), and their related fluxes, refer to position and transport *within* the flux surface.

From the point of view of turbulence, a more important quantity is the radial gradient of the diamagnetic velocity, $\nabla_\perp u_\wedge$. This is largest in the near-SOL region where strong radial electric fields are present; in §3 the E-field was estimated as $E_\perp \sim 3\nabla_\perp T_e \sim 3T_e/\lambda_{Te}$, where $\lambda_{Te} \equiv |\nabla_\perp T_e/T_e|^{-1}$ is the electron temperature gradient length evaluated at the outer target, which is typically somewhat larger than the power width $\lambda_{Te} \sim (2-3)\lambda_q$. The resulting **E×B** velocity is mostly in the diamagnetic direction, and can be estimated as $u_E \sim u_\wedge \sim E_\perp/B \sim 3T_e/B\lambda_{Te} \sim 10$km/s or $u_\wedge/c_s \sim 0.1$ for typical JET near-SOL conditions; it has been already discussed in the context of the classical drift effects in the SOL, §3 and Fig.10. The radial gradient of this velocity,

$$\nabla_\perp u_\wedge \sim u_\wedge/\lambda_{Te} \sim 3T_e/B\lambda_{Te}^2 \tag{5.19}$$

produces a stretching or shearing of the filaments, which reduces the radial correlation length of turbulence and the associated time-averaged radial fluxes. This mechanism has been demonstrated in turbulence simulations and is almost certainly responsible for the formation of the edge transport barrier; it is also the most likely explanation for the reduction of radial transport in the near-SOL, where the velocity shear $\nabla_\perp u_\wedge$ is strongest.

Following Appendix A, we define the shearing or eddy turn-over time, $\tau_u \sim \delta_\wedge/\Delta u_\wedge \sim \delta_\wedge/\delta_\perp \, {}_\perp u_\wedge$ as the time taken to stretch the filament in the diamagnetic direction to twice its original size. Assuming a background electric field, this time becomes $\tau_u \sim (\delta_\wedge/u_\wedge)(\lambda_{Te}/\delta_\perp)$. It should be compared with the parallel loss time $\tau_{||} \sim \delta_{||}/u_{||}$, cf. (5.10). Their ratio measures the relative importance of the two effects,

$$\tau_{\nabla u}/\tau_{||} \sim (\delta_\wedge/\delta_{||})(u_{||}/u_\wedge)(\lambda_{Te}/\delta_\perp) \tag{5.20}$$

Shearing effects dominate when $\tau_{\nabla u}/\tau_{\|} < 1$. To evaluate this further we consider the case of convective losses, $u_{\|} \sim c_s$ and $u_{\wedge} \sim 0.1c_s$, such that $\delta_{\wedge}/\delta_{\|} < 0.1(\delta_{\perp}/\lambda_{Te})$. If we assume the filaments are smaller than the profile width, $\delta_{\perp}/\lambda_{Te} < 1$, we find $\delta_{\wedge}/\delta_{\|} < 0.1$ for the largest filaments in the near-SOL. Considering fully elongated filaments, $\delta_{\|} \sim L_{\|} \sim 50$ m [Thomsen02], this translates into $\delta_{\wedge} < 5$m, which is comparable to the poloidal extent of the SOL, $L_{\wedge} \sim 2\pi r_{sep} \sim 6$m. In other words, plasma eddies in the near-SOL are not only highly elongated in the parallel direction and resemble 1-D filaments, but also effectively stretched in the diamagnetic direction, such that they begin to approximate 2-D plasma sheets, flattened within the flux surface; this change in the eddy topology is common in both fluid and MHD turbulence. The smaller the radial extent of the 1-D filament in comparison to the radial gradient length of the electric field, the faster is it stretched into such a 2-D plasma sheet. As a consequence, we expect only weak gradients within the flux surface itself, at least in the near-SOL region, which justifies the neglect of $u_{\wedge}$ and $q_{\wedge}$, and the choice of radial diffusion as the dominant collisional loss mechanism.

5.5 THERMAL ENERGY DISSIPATIVE SCALES

In the previous sections we obtained expressions for the dissipative times due to energy losses in the $\|$, $\wedge$ and $\perp$ directions. We are now ready to derive the dissipative scale $l_{\perp\sigma}$ based on the balance of $\perp$ and $\|$ losses of thermal energy of species σ in the filament frame of reference. These are comparable when

$$\Theta_\sigma \equiv \nabla_\perp q_{\perp\sigma}/\nabla_\| q_{\|\sigma} = \tau_{\|\sigma}/\tau_{\perp\sigma} \sim 1 \tag{5.21}$$

We could of course consider all three effects discussed above: parallel loss §5.2, radial diffusion §5.3 and diamagnetic shear §5.4, and define corresponding dissipative scales by equating each of these in turn. However, in the light of the discussion in §5.4, we will restrict ourselves to considering the balance of radial and parallel losses alone; the inclusion of diamagnetic transport does not substantially change the results of the analysis, while greatly complicating the algebra. In other words, we will adopt (5.21) as the definition of $l_{\perp\sigma}$ which measures the smallest coherent structures in energy density and/or the smallest (radial) gradient length in the filament frame; the subscript $\perp$ indicates that $l_{\perp\sigma}$ measures a *radial* length. Using (5.10), (5.16) and (5.21) yields an estimate of the dissipative scale for species σ,

$$l_{\perp\sigma} \sim (2/3\times\chi_{\perp\sigma}\tau_{\|\sigma})^{1/2} \sim \rho_\sigma(2/3\times c_{\perp\sigma}N_{\perp\sigma})^{1/2} \tag{5.22}$$

where $N_{\perp\sigma} = \tau_{\|\sigma}/\tau_{\sigma\sigma}$ is the average number of $\perp$ diffusive steps per $\|$ transport time of species σ. In other words, $l_{\perp\sigma}$ is equal to ρ_σ multiplied by some factor of order $N_{\perp\sigma}^{1/2}$ which leads to collisional broadening. The parametric dependence of this and other related expressions are discussed in more detail in Appendix B. On physical grounds, both $l_{\perp\sigma}$ and/or $\lambda_{T\sigma} \equiv |T_\sigma/\nabla_\perp T_\sigma|$ cannot be smaller than

ρ_σ, which follows directly from the assumption of strong magnetisation of the plasma, $\min(\omega_{c\sigma}\tau_{\sigma\sigma}, \omega_{c\sigma}\tau_{\|\sigma}) >> 1$ (the velocity distribution, $f_\sigma(\mathbf{v})$ and all its moments, including the energy ε_σ, are quickly ($\sim\omega_{c\sigma}^{-1}$) broadened over a radial extent of the gyration, that is over ρ_σ). We will therefore replace (5.22) by,

$$l_{\perp\sigma}/\rho_\sigma \sim \max\{1, (2/3\times c_{\perp\sigma}N_{\perp\sigma})^{1/2}\} \geq 1 \qquad (5.23)$$

Since we are ultimately interested in the ratio of ion and electron dissipative scales, $l_{\perp i}/l_{\perp e}$, we combine (5.23) with the ratio of ion and electron gyro-radii $\rho_i/\rho_e = (\vartheta m_i/m_e)^{1/2} \sim 60\times(T_i/T_e)^{1/2} \sim O(10^2)$ for D^+, and plot the result vs. electron collisionality in Fig.15. The interval, $1 < \nu^*_e < 10^3$, has been chosen to span the range of $\nu^*_i = \nu^*_e\vartheta^{-2}$ of Fig.14. For typical JET near-SOL conditions, shown as a shaded region in Fig.15, $l_{\perp i}$ exceeds $l_{\perp e}$ by roughly an order of magnitude, $l_{\perp i}/l_{\perp e} \sim 7\text{-}20 \sim O(10)$. Similar values are found for Alcator C-Mod [LaBombard97] and ITER [ITER99]: $(l_{\perp i}/l_{\perp e})^{\text{C-Mod}} \sim 4\text{-}20$ and $(l_{\perp i}/l_{\perp e})^{\text{ITER}} \sim 8\text{-}20$.

We can now rewrite the balance of radial and parallel losses of thermal energy in the filament frame of reference (5.21), using (5.10) and (5.23), as

$$\Theta_\sigma \equiv \nabla_\perp q_{\perp\sigma}/\nabla_\| q_{\|\sigma} = \tau_{\|\sigma}/\tau_{\perp\sigma} = (l_{\perp\sigma}/\delta_\perp)^2 \qquad (5.24)$$

which scales as the inverse square of the filament size $\delta_\perp$ normalised to $l_{\perp\sigma}$. In other words, collisional diffusion is negligible for filaments much larger than the dissipative scale; its relative importance increases quadratically as the filament size is reduced. Consequently,

$$\Theta_i/\Theta_e = (l_{\perp i}/l_{\perp e})^2 \sim O(10^2) \qquad (5.25)$$

and the ion to electron ratio of the relative strength of radial and parallel thermal energy loss mechanisms is found to be independent of the scale considered, being determined solely by the square of the ratio of their dissipative scales, see Fig.15. For estimated JET near-SOL conditions, (5.25) predicts $\Theta_i/\Theta_e \sim 50\text{-}400 \sim O(10^2)$. Therefore, irrespective of the size of the filament considered, collisional losses of thermal energy by radial heat conduction are always much larger for ions than electrons. This is the anticipated result in light of $\chi_{\perp i}/\chi_{\perp e} >> 1$, however, by including the details of parallel transport and performing a sensitivity study to several plasma variables, it has now been established for a wide range of near-SOL conditions, including those relevant to JET and ITER.

We have seen above that collisional effects only become important at filament scales $\delta_\perp$ comparable to $l_{\perp\sigma}$. As we consider filaments of progressively smaller size, this condition will first be satisfied for the ions, since $l_{\perp i} >> l_{\perp e}$. At the scale $\delta_\perp \sim l_{\perp i}$, the ion thermal energy evolution is affected by ion-ion collisions (classical $\chi_{\perp i}$), $\Theta_i \sim 1$, while the electron thermal energy remains largely unaffected by electron-electron collisions (classical $\chi_{\perp e}$), $\Theta_e \sim O(10^{-2})$. Consequently, the perpendicular ion

energy transport is dominated by collisional heat diffusion, while electron energy transport is still governed by turbulent convection in the $\perp$-$\wedge$ plane. In other words, collisional diffusion dominates the radial energy transport of ions, and turbulent convection that of electrons. If a finite level of turbulent convection is included, $u_\perp > 0$, the radial fluxes of thermal energy and the resulting power profiles, involve both collisional and turbulent contributions, but due to (5.25), their ratio is always bigger for ions.

To relate the above conclusions to the experimental results presented in Sections 2 to 4, we need only note that the typical power widths measured in the JET near-SOL are in fact comparable to the ion dissipative scale, $\lambda_q \sim O(l_{\perp i})$. Therefore, the conclusions of the previous paragraph should be directly applicable to JET plasmas discussed in this study. With the value of $u_\perp \sim 10$m/s inferred in the near-SOL, we can conclude that turbulent radial convection is much weaker than collisional, (neo)-classical ion heat conduction, i.e. collisional diffusion dominates the radial transport of ion energy in the near-SOL. This is the key result of the analysis presented in this section.

We close the section with a brief summary and an overview of this analysis. It was shown in Sections 5.2-5.4, that the energy evolution of a SOL turbulent filament is influenced by three processes: parallel loss to the targets, radial heat diffusion and poloidal velocity shear. The latter is the most difficult to quantify; it generally leads to filament break up (or flattening into a 2-D plasma sheet) and thus a redistribution of thermal energy within the flux surface, with little effect on average radial profiles. The dissipative scale, $l_{\perp\sigma}$, defined as the scale at which parallel and radial energy losses from an filament of arbitrary size are comparable, is roughly equal to the diffusive length for each species, $l_{\perp\sigma} \sim \rho_\sigma \nu^{*1/2}_\sigma$, such that $l_{\perp i} >> l_{\perp e}$, Fig.15. The ion dissipative scale is therefore comparable to the measured SOL power width $\lambda_q \sim O(\lambda_q^{A1}) \sim O(l_{\perp i})$, while $l_{\perp e}$ is an order of magnitude smaller. As such, radial heat conduction due to ion-ion collisions is at least comparable to turbulent convection of *ion* thermal energy for typical SOL turbulence scales, but has little effect on the transport of particles, momentum or *electron* thermal energy. In contrast, heat diffusion due to electron-electron collisions is much smaller than turbulent convection of *electron* thermal energy. In other words, for the level of turbulence implied in the near-SOL of JET H-modes, collisional (conductive) and turbulent (convective) transport processes are dominant for ions and electrons, respectively. This is made possible by the fact that under typical JET near-SOL conditions, electrons are collisional ($\nu_e^* \sim 25$), but are effectively thermally decoupled from the ions ($\nu_{ie}^* \sim 0.5$). Consequently, the ion and electron energy transport can proceed by separate channels and be governed by largely independent mechanisms. The same cannot be said for the transport of mass and, to a lesser extent momentum, which are intimately linked for both species via the quasi-neutrality condition resulting in the ambipolar flux constraint.

With these conclusions, a general picture of inter-ELM energy transport in the SOL emerges in which SOL turbulence in the near-SOL is reduced by poloidal velocity shear (vorticity), but is not entirely suppressed. The turbulence level is low enough and the radial gradients steep enough, for (neo-)classical ion conduction to dominate the radial ion energy transport. Turbulence simulations

have demonstrated this self-regulating reduction in radial transport, although an exhaustive treatment of collisional, dissipative effects in SOL turbulence codes is still lacking at present.

CONCLUSIONS

Significant progress has been made in understanding power exhaust mechanisms on JET under ITER-relevant conditions. Analysis of measured ELM-averaged divertor power deposition profiles for a range of plasma conditions in both forward and reversed toroidal field direction, suggests that near-SOL poloidal energy transport (i.e. transport of thermal energy within the flux surface) is governed largely by classical physics: in the parallel (||) direction by classical heat conduction and convection, in the diamagnetic ($\wedge$) direction by classical (guiding centre and diamagnetic) drifts. In contrast, near-SOL radial energy transport (i.e. transport of thermal energy normal ($\perp$) to the flux surface) is determined by a combination of collisional and turbulent processes, with transport of *ion energy* as the dominant channel. Comparison of the JET experiments with theories of radial heat diffusivity suggests that ELM-averaged radial energy transport is dominated by *(neo-)classical* ion conduction, including *collisional* ion orbit loss; the term *(neo-)classical* denotes an intermediate regime between classical and neo-classical (Pfirsch-Schlueter) diffusion, which reflects the change of magnetic topology at the separatrix. A similar experiment-theory comparison for both *upstream* and *downstream* electron power profiles on JET and AUG, indicates that *electron energy* transport in both machines is dominated by turbulent convection, most likely driven by MHD interchange and drift-Alfven instabilities.

The co-existence of turbulent convection for electron energy and collisional conduction for ion energy can be reconciled by considering the phenomenology of SOL plasma turbulence, including its dissipative properties. Such analysis allows us to form a coherent picture of ELM-averaged power exhaust which may be summarised as follows: the growth of strong radial electric fields and poloidal velocity shear in the near-SOL during the inter-ELM H-mode phase results in a strong reduction of radial turbulent convection in that region. As the strength of the H-mode barrier increases, ion and electron collisionalities are reduced and the relative importance of poloidal drift effects increases. Based on the measured profiles, we infer that ion-ion collisions compete with turbulent convection as the dominant transport mechanism in the near-SOL. Since radial heat diffusion is much faster for ions than for electrons – a direct consequence of the larger ion gyro-radius – the role of electron-electron collisions and electron heat diffusion is negligible. These effects can be expressed in terms of the relative magnitude of SOL dissipative scales, which are defined as the radial lengths at which the convective and collisional fluxes are equal. The ion dissipative scale is found to be comparable to the measured target power profiles, while the electron scale is roughly an order of magnitude smaller. This explains why collisional effects play an important role in ion, but not in electron radial energy transport.

It is at present not possible to clearly differentiate between inter-ELM and ELM contributions to ELM-averaged power deposition profiles on JET. The difficulties include: 1) insufficient diagnostic

accuracy, 2) little, if any, profile broadening due to the ELMs, 3) insufficient power to achieve Type-I ELMs in He experiments, and 4) a strong correlation between collisionality and ELM size. Until these problems can be overcome, it is difficult to confidently isolate specific ELM contributions. For example, the excess heat load and peaked profile shape in Type-I ELMy H-modes may be explained by either inter-ELM energetic ions or energetic ions and electrons associated with the ELMs. Likewise, the beneficial effect of fuelling in reducing the peak divertor heat load can be accounted for either by the increase in the ion collisionality and its effect on inter-ELM transport or by the related reduction in the ELM size. Further experiments and simulations are required to clarify the above issues.

The results of this study may be used to predict ELM-averaged power exhaust on ITER, by extrapolating from the JET results using the best-fit empirical scalings and leading candidate theories. Thus, extrapolating from JET Pulse No: 50397 (16MW NBI, 2.5MA/2.4T) using expressions (2.4) to (2.6) and expected separatrix values on ITER ($n_{e,sep} = 3\times10^{19}\,m^{-3}$, $2T_{e,sep} = T_{i,sep} = 400$ eV, $\nu^*_{i,sep} \sim 1.1$), we find an integral power width of $\lambda_q^{ITER} \sim 3.7 \pm 1.1$mm mapped to the outer mid-plane, which is comparable to $\rho_{\theta i}$ evaluated at the separatrix. Due to the low separatrix ion collisionality, we expect the peak heat load to be dominated by the excess contribution, $q_{tot} - q_{e,inter\text{-}ELM}$, which in Section 2 we identified with the energetic ion component. Since JET results are based primarily on natural density H-modes under attached divertor conditions, the above estimate of λ_q^{ITER} should be viewed as the power width at the *entrance* to the ITER divertor throat, eg. at the height of the X-point [Fundamenski04]. We expect this profile to be significantly broadened by ion-ion and charge-exchange collisions in the dense plasma in the V-shaped ITER divertor, where partially detached operation is essential, such that target λ_q exceeds the ITER design value of 5mm [Kukushkin02, ITER99]. It is worth noting that existing modelling of ITER divertor operation neglects all effects associated with classical drifts in the SOL. Based on the work reported here, we anticipate that these effects will increase the poloidal power flow into the outer divertor and thereby reduce the degree of detachment in that leg. It thus appears timely to revisit these simulations with the effect of classical drifts included. Finally, the analysis and conclusions of Section 5 remain valid for ITER with an anticipated ratio of ion and electron thermal energy dissipative scales in the range of $(l_{\perp i}/l_{\perp e})^{ITER} \sim$ 8-20.

ACKNOWLEDGEMENT

This work was conducted under European Fusion Development Agreement and was partly funded by EURATOM and the United Kingdom Engineering and Physical Sciences Research Council. We would like to thank J. Connor, E.O. Garcia, A. Loarte, V. Naulin and B. Scott for many helpful comments and discussions.

APPENDIX A: THE CONCEPT OF THE DISSIPATIVE SCALE

The dissipative scale is a well established concept in hydrodynamic turbulence theory. It can be traced to Kolmogorov's phenomenology of turbulence [Kolmogorov41], a clear account of which may be found in [Kadomtsev65, Tennekes72, Frisch95, Biskamp03]. In this picture, a turbulent flow is represented as a collection of different sized coherent structures (traditionally called eddies, whirls or vortices), which interact through the non-linear, advective term in the Navier-Stokes equation; this interaction leads to the distortion and eventual break-up of larger into ever smaller eddies, a process known as the Richardson

eddy cascade. The range of scales at which these interactions dominate forms the *inertial range.* If kinetic energy is injected at the largest scales, say by stirring the fluid, the energy is then transported by non-linear interactions to ever smaller scales throughout the inertial range; when the eddies become sufficiently small, their kinetic energy is converted into thermal energy (or dissipated) by viscous heating associated with inter-particle collisions. The scale at which collisional and inertial effects are comparable is known as the *dissipative scale* l_ν, and determines the smallest scale at which coherent structures (eddies) can exist in the flow.

The dissipative scale l_ν was derived by Kolomogorov on dimensional grounds for the highly idealised case of fully developed, incompressible, homogenous, isotropic, three dimensional turbulence. At this scale the inertial $\boldsymbol{u}\cdot\nabla\boldsymbol{u}$ and viscous $\nu\nabla^2\boldsymbol{u}$ terms in the Navier-Stokes equation,

$$\partial\boldsymbol{u}/\partial t + \boldsymbol{u}\cdot\nabla\boldsymbol{u} = -\nabla p + \nu\nabla^2\boldsymbol{u} \tag{A.1}$$

are comparable; here $\boldsymbol{u}$ is the velocity and ν the kinematic viscosity. Their ratio defines the Reynolds number $\mathrm{Re} = \tau_\nu/\tau_u$, where τ_u and τ_ν are the characteristic advective and collisional (viscous) times. For a eddy of size δ, these may be estimated by replacing the gradient by the inverse of the eddy size ($\nabla \rightarrow \delta^{-1}$), such that $\tau_u \sim \delta/u$ and $\tau_\nu \sim \delta^2/\nu$, and $\mathrm{Re} = \mathrm{Re}(\delta)$. The dissipative scale can thus be defined as,

$$\mathrm{Re}(l_\nu) \sim 1 \quad \Rightarrow \quad l_\nu \sim \nu/u_\nu \tag{A.2}$$

where u_ν is a characteristic velocity at the scale $\delta = l_\nu$. Since $\mathrm{Re} > 1$ in the inertial range ($\delta > l_\nu$), dissipative effects may be ignored throughout most of the eddy energy cascade. With no dissipation taking place in the inertial range, all the energy injected at large scales is transported to the dissipative scale. The rate of energy injection per unit mass ε can therefore be written as $\varepsilon \sim u^2/(\delta/u) \sim u^3/\delta \sim u_\nu^3/l_\nu$ [Tennekes72, Frisch95], which by (A.2) yields an expression for l_ν in terms of ν and ε,

$$l_\nu \sim \nu/u_\nu \sim (\nu^3/\varepsilon)^{1/4} \tag{A.3}$$

In this simple formulation l_ν depends only on the collisional interactions (ν) and the kinetic energy injected into the system at the largest scales (ε), not on the details of the flow pattern ($\boldsymbol{u}$). Consequently, l_ν can be calculated entirely within the eddy frame of reference, which circumvents the non-linear advection terms and substantially simplifies the analysis (from differential to algebraic equations); in this frame, τ_u represents the eddy turn-over time (in which the eddy is destroyed by velocity shear) and τ_ν the viscous time (in which momentum diffuses out of the eddy volume). The dissipative scale l_ν also determines the smallest gradient length likely to exist in the fluid; as a result, the power spectrum of turbulent fluctuations E(k), which scales as $k^{-5/3}$ in the inertial range, falls off more rapidly for $k > k_\nu \sim l_\nu^{-1}$ [Frisch95].

In the above formulation, kinetic energy dissipation occurs via collisional diffusion of momentum out of the eddy volume. Similarly, one could formulate dissipative scales for a passive scalar, such as a tracer concentration or the fluid temperature. In the latter case, the thermal energy dissipation (reduction of eddy stored energy) occurs via collisional heat diffusion out of the eddy volume, and the kinematic viscosity ν is replaced by the heat diffusivity χ.

If the flow is two, rather than three dimensional, the conservation of vorticity provides an additional invariant and leads to a positive (larger to smaller scales) cascade of enstrophy and an inverse (smaller to larger scales) cascade of kinetic energy [Tennekes72, Frisch95]. The inverse energy cascade results in formation of large scale structures which terminate at some system related scale. The injection of kinetic energy at rate ε is accompanied by the injection of enstrophy at rate ε_Ω, both occurring at the same length scale. On dimensional grounds, similar to those employed to derive (A.3), the enstrophy dissipation length is found as

$$l_\Omega \sim (\nu^3/\varepsilon_\Omega)^{1/6} \tag{A.4}$$

while the power spectrum of turbulent fluctuations E(k) in the enstrophy cascade scales as k^{-3}. Despite these differences, the concept of a dissipative scale is equally applicable to both two and three dimensional turbulence.

In the context of magnetised plasma turbulence, which can be treated as quasi two-dimensional with advective motions in the $\perp$-$\wedge$ plane, see Section 4, the dissipative scale defines some perpendicular length at which collisional and interial forces are equal. In the SOL, where the strongest gradients occur normal to the flux surfaces, we expect the dissipative scale to define the smallest radial gradient length, $\lambda_\psi \equiv |\psi/\nabla_\perp \psi|$, where $\psi \in \{n, T_e, T_i\}$. It is worth noting that the SOL has the structure of a thin, elongated boundary layer with $\lambda_\psi << L_\parallel$, and such that we expect SOL plasma *eddies* to correspond to highly elongated *filaments* [Biskamp03, Taylor97, Naulin02, Antar01, Thomsen02]. When averaged over all scales, filament motions in the $\perp$-$\wedge$ plane result in a net radial flux of particles and energy. In addition to collisional diffusion, parallel losses to the divertor targets and diamagnetic velocity shear also produce an effective dissipation mechanisms. The SOL

dissipative scale must therefore account for losses in all three magnetic directions, although we expect || and ⊥ losses to dominate.

For the purpose of characterising power exhaust, which is the topic of the present article, we are primarily interested in the transport of thermal energy (heat) rather than kinetic energy or momentum. In the ⊥-∧ plane, thermal energy is both convected by turbulent motions and conducted (diffused) by collisions. However, due to a strong dependence of the Coulomb collision cross-section on temperature, thermal energy cannot be treated simply as a *passive* scalar embedded in the flow. Instead, temperature should be treated as an *active* scalar, which somewhat complicates the analysis. As mentioned previously, the heat diffusivity χ replaces the kinematic viscosity ν as the relevant collisional diffusivity, such that the dissipative scale l_ν becomes l_χ. This scale now determines the smallest radial *temperature* gradient length likely to exist in the plasma. Since $\chi_{\perp i} >> \chi_{\perp e}$ on account of the larger ion gyro-radius, we expect this scale to be much larger for ions than electrons.

APPENDIX B: PARAMETRIC ANALYSIS OF THE DISSIPATIVE SCALE (5.22)

Below we investigate the parametric dependence of (5.22). Using (5.10), $N_{\perp\sigma}$ can be written as a product of two terms

$$N_{\perp\sigma} = 3/5\times(\tau_{\chi\|\sigma}/\tau_{\sigma\sigma})\times(1 + \tau_{\chi\|\sigma}/\tau_{\nu\|})^{-1} \tag{B.1}$$

The first term $\tau_{\|\sigma}/\tau_{\sigma\sigma}$, which can be interpreted as the average number of ⊥ diffusive steps per || conductive time $N_\perp{}^\chi{}_\sigma$, is found from (5.10) and (5.13) as

$$N_\perp{}^\chi{}_\sigma = \tau_{\|\sigma}/\tau_{\sigma\sigma} = \nu^*{}_\sigma{}^2\times(1 + \nu^*{}_\sigma{}^c/\nu^*{}_\sigma)/c_{\|\sigma} \tag{B.2}$$

This reduces to $\nu^*{}_\sigma/\alpha_\sigma \propto T_\sigma{}^{-2}$ and $\nu^*{}_\sigma{}^2/c_{\|\sigma} \propto T_\sigma{}^{-4}$, for $\nu^*{}_\sigma << \nu^*{}_\sigma{}^c$ and $\nu^*{}_\sigma >> \nu^*{}_\sigma{}^c$, respectively; here we made use of (5.12) to make the T_σ dependence explicit. The ratio of electron and ion steps, $N_\perp{}^\chi{}_e/N_\perp{}^\chi{}_i$, is thus found as $5\times\vartheta^2 \sim$ 5-50 and $1.2\times\vartheta^4 \sim$ 1.2-100 in the two limits, with the range of values for $1 < \vartheta < 3$ indicated.

The second term in (B.1) represents the convective contribution to || energy loss and has already been formulated in (5.14). Inserting (5.14) and (B.2) into (B.1), gives the final expression

$$N_{\perp\sigma} = 3/5\times\nu^*{}_\sigma\times\{c_{\|\sigma\sigma}(\nu^*{}_\sigma + \nu^*{}_\sigma{}^c)^{-1} + 5/2\times M\xi(v_{ti}/v_{t\sigma})\}^{-1} \tag{B.3}$$
$$\nu^*{}_\sigma{}^c = c_{\|\sigma}/\alpha_\sigma, \quad \xi = (1 + Z/\vartheta)^{1/2}, \quad v_{ti}/v_{t\sigma} = (T_i/T_\sigma)^{1/2}(m_i/m_e)^{-1/2}$$

which depends on three dimensionless parameters: $\nu^*{}_\sigma$, ϑ and M. We now consider the three asymptotic limits of (B.3):

- the *collisional, conductive* limit ($M << M^c{}_\sigma$, $\nu^*{}_\sigma >> \nu^*{}_\sigma{}^c$) in which (B.2) reduces to $3/5\times N_\perp{}^\chi{}_\sigma$ as found in (B.2),

$$N_{\perp\sigma} = 3/5\times\nu^{*}_{\sigma}{}^{2}/c_{\|\sigma\sigma} \propto T_{\sigma}^{-4} \tag{B.4}$$

- the *free-streaming, conductive* limit ($M << M^{c}_{\sigma}$, $\nu^{*}_{\sigma} << \nu^{*}_{\sigma}{}^{c}$) in which (B.2) once again applies, but now yields

$$N_{\perp\sigma} = 3/5\times\nu^{*}_{\sigma}/\alpha_{\sigma} \propto T_{\sigma}^{-2} \tag{B.5}$$

- the *convective* limit ($M >> M^{c}_{\sigma}$), which based on Fig.14 only applies for ions in the SOL; in this limit (B.1) reduces to

$$N_{\perp\sigma} = 3/5\times\nu^{*}_{\sigma}\{5/2\times M\xi(v_{ti}/v_{t\sigma})\}^{-1} \tag{B.6}$$
$$\therefore N_{\perp i} = 6/25\times\nu^{*}_{i}/M\xi \propto T_{i}^{-2}/M(1 + Z/\vartheta)^{1/2}$$

In short, $N_{\perp\sigma}$ increases monotonically with the filament collisionality ν^{*}_{σ}: quadratically in the collisional conductive limit ($M << M^{c}_{\sigma}$, $\nu^{*}_{\sigma} >> \nu^{*}_{\sigma}{}^{c}$) and linearly in the conductive, free streaming ($M << M^{c}_{\sigma}$, $\nu^{*}_{\sigma} << \nu^{*}_{\sigma}{}^{c}$) or convective ($M >> M^{c}_{\sigma}$) limits. The ratio $N_{\perp e}/N_{\perp i}$ in the three asymptotic limits is shown in Table 3; since electron transport is firmly fixed in the conductive regime ($M < M^{c}_{e}$, Fig.14), the electron convective limit ($M >> M^{c}_{e}$) has been omitted from Table 3.

Based on the asymptotic behaviour of $N_{\perp\sigma}$, (B.4)-(B.6), we expect $l_{\perp\sigma}/\rho_{\sigma}$ to increase monotonically with ν^{*}_{σ} for all values of ϑ and M: linearly for ($M << M^{c}_{\sigma}$, $\nu^{*}_{\sigma} >> \nu^{*}_{\sigma}{}^{c}$) and as a square-root for ($M << M^{c}_{\sigma}$, $\nu^{*}_{\sigma} << \nu^{*}_{\sigma}{}^{c}$) or ($M >> M^{c}_{\sigma}$), see Fig.A.1.

The expression (5.23) is plotted in Fig.A.1 for a range of ν^{*}_{σ} over a range of $1 < \vartheta\ (=T_i/T_e) < 10$ and $0.01 < M < 1$. The electron ratio $l_{\perp e}/\rho_e$ is largely insensitive to both ϑ and M in this range, increasing from ~1 for $\nu^{*}_{e} \sim 0.1$ to ~30-100 for $\nu^{*}_{e} \sim 10^3$. Similarly, $l_{\perp i}/\rho_i$ is insensitive to ϑ but is noticeably reduced with increasing M, increasing from ~1 for $\nu^{*}_{i} \sim$ 1-3 to ~20-200 for $\nu^{*}_{i} \sim 10^3$. Finally, we find $l_{\perp i}/\rho_i < l_{\perp e}/\rho_e$ provided that $\nu^{*}_{\sigma} < 30$. Although $l_{\perp\sigma}/\rho_{\sigma}$ depends on ν^{*}_{σ} along with two other parameters (ϑ, M), the ratio $(l_{\perp i}/\rho_i)/(l_{\perp e}/\rho_e)$ depends on only three parameters (ν^{*}_{e}, ν^{*}_{i}, M) or (ν^{*}_{e}, ϑ, M), since the two collisionalities are related via (5.12), i.e. $\nu^{*}_{e} = \vartheta^2\nu^{*}_{i}$. For $\nu^{*}_{e} \sim 0.1$, $(l_{\perp i}/\rho_i)/(l_{\perp e}/\rho_e) \sim 1$ for all ϑ and M. As ν^{*}_{e} increases, $(l_{\perp i}/\rho_i)/(l_{\perp e}/\rho_e)$ decreases uniformly with little effect of ϑ and M, until $\nu^{*}_{e}\vartheta^{-2} = \nu^{*}_{i} \sim 1$. Thereafter, $(l_{\perp i}/\rho_i)/(l_{\perp e}/\rho_e)$ remains roughly constant at its $\nu^{*}_{i} \sim 1$ value for moderate Mach numbers, with some decrease close to sonic velocities. For estimated JET near-SOL conditions ($10 < \nu^{*}_{e} < 30$, $1 < \vartheta < 3$, $0.03 < M < 0.3$), we find $(l_{\perp i}/\rho_i)/(l_{\perp e}/\rho_e) \sim 0.07$-$0.3$.
The ratio of dissipative un-normalised scales $l_{\perp i}/l_{\perp e}$, plotted in Fig.15, exhibits qualitatively similar behaviour, with a few marked dfferences:

- $l_{\perp i}/l_{\perp e} > 1$ over the entire range of ν^{*}_{e}, ϑ and M
- For $\nu^{*}_{e}\vartheta^{-2} = \nu^{*}_{i} < 1$, $l_{\perp i}/l_{\perp e}$ does not approach a common value but increases as $\sim\vartheta^{1/2}$ at fixed ν^{*}_{e}, with little effect of M.
- The value of $l_{\perp i}/l_{\perp e}$ at $\nu^{*}_{e}\vartheta^{-2} = \nu^{*}_{i} \sim 1$ decreases less than linearly with ϑ
- For $\nu^{*}_{e}\vartheta^{-2} = \nu^{*}_{i} > 1$, $l_{\perp i}/l_{\perp e}$ stays roughly constant at its $\nu^{*}_{i} \sim 1$ value for moderate Mach numbers, with a mild decrease close to the sonic boundary.

For estimated JET near-SOL conditions, shown as a shaded region in Fig.15, we find $l_{\perp i}/l_{\perp e} \sim$ 7-20 ~ O(10), such that $l_{\perp i}$ exceeds $l_{\perp e}$ by roughly a factor of ten, which is less than the ratio of the gyro radii $\rho_i/\rho_e \sim O(10^2)$, but still much larger than unity.

APPENDIX C: LIST OF SYMBOLS

C.1 SPECIAL SYMBOLS

$\langle\cdot\rangle$	volume average
$\|, \wedge, \perp$	parallel, diamagnetic and radial directions

C.2 GREEK SYMBOLS: $\sigma \in \{i,e\}$ IS A SPECIES INDEX

α_σ	free streaming multiplier (for species σ)
$\chi_{\|\sigma}$	parallel heat diffusivity
$\chi_{\|\sigma}^{SH}$	Spitzer-Harm parallel heat diffusivity
$\chi_{\perp\sigma}$	radial heat diffusivity
$\chi_\perp$	total (ion + electron) radial heat diffusivity
$\chi_{\perp i}^{PS}$	Pfirsch-Schlueter radial ion heat diffusivity
$\chi_{\wedge\sigma}$	diamagnetic heat diffusivity
χ_B	Bohm diffusivity, $\chi_B \sim T_e/B$
$\delta_\|, \delta_\wedge, \delta_\perp$	size of the eddy (filament)
ε_σ	filament energy density, $\varepsilon_\sigma \sim n(3/2\times T_\sigma + 1/2\times m_\sigma u_\|^2)$
$\varepsilon = a / R$	aspect ratio
ε	energy injection rate per unit mass
ε_Ω	enstrophy injection rate per unit mass
ϕ, θ, r	toroidal, poloidal and radial directions
Φ	net flux expansion factor, $\Phi = ds_t/dr_u$
γ_σ	sheath energy transmission coefficient
Γ_o/Γ_I	outer/inner deposited particle fluxes
$\boldsymbol{\kappa} = (\mathbf{b}\cdot\nabla)\mathbf{b}$	curvature vector
λ_q	integral power width, $\lambda_q \equiv \int qdr /q_0$
$\lambda_q^{all}, \lambda_q^{H}$	power width regressing with all data /only H-mode shots
$\lambda_q^{X\text{-}\nu^*}$	collisional IOL width, as defined by (2.6)
$\lambda_{T\sigma}$	temperature gradient length,
$\lambda_{\sigma\sigma}$	mean-free-path,
$\lambda_q^{\nu} = \lambda_q(\tau_{\|\nu})$	convectively dominated parallel transport width
$\lambda_q^{\chi} = \lambda_q(\tau_{\|\chi})$	conductively dominated parallel transport width
$\mu \in \{\|, \wedge, \perp\}$	directional index
ν_σ	characteristic collision frequency

ν_σ^*	collisionality, $\nu_\sigma^* \equiv L_\parallel/\lambda_{\sigma\sigma}$
$\nu^*{}_\sigma^c = c_{\parallel\sigma}/\alpha_\sigma$	critical collisionality
$\vartheta \equiv T_i/T_e$	ion-to-electron temperature ratio
$\theta_\perp$	field line inclination angle at the target
θ_0	poloidal launch location
Θ_σ	defined by (5.21)
$\rho_{\theta i}$	poloidal ion gyro-radius
$\rho_{\theta s}$	poloidal gyro-radius evaluated at the sound speed
ρ_0	radial launch location
ρ_σ	thermal gyro-radius $\sigma \in \{i,e\}$ species index
τ_{ie}	ion-electron energy equilibration time
$\tau_{\sigma\sigma}$	characteristic collision time for σ-σ Coulomb scattering
$\tau_{\mu\sigma}$	characteristic energy transport (or loss) time
τ_u	shearing or eddy turn-over time, $\tau_u \sim \delta_\wedge/\Delta u_\wedge$
$\tau_{\parallel\nu}$ and $\tau_{\parallel\chi}$	convective and conductive energy loss times,
$\tau_\parallel$	harmonic average of the two
τ_u, τ_ν	characteristic advective and collisional (viscous) times
$\omega_{c\sigma}$	gyro-frequency for species σ
ξ	defined by $\xi \equiv (1+Z/\vartheta)^{1/2}$
ζ	transitional variable, $\zeta \equiv \nu^*_i / (1 + \nu^*_i)$

C.3 LATIN SYMBOLS: BOLD CAPITALS REPRESENT THEORIES OF RADIAL ENERGY TRANSPORT

a	minor radius
A	atomic mass of main plasma ions
A1	classical ion heat conduction, $\chi_\perp^{A1} \propto \rho_i^2 \nu_i$
A2	neo-classical ion heat conduction, $\chi_\perp^{A2} \propto \chi_\perp^{A1}(B/B_\theta)^2 \propto \rho_{\theta i}^2 \nu_i$
A3	classical electron heat conduction, $\chi_\perp^{A3} \sim \chi_\perp^{A1}(m_e/m_i)^{1/2} \propto \rho_e^2 \nu_e$
B1, **B2**	endplate MHD interchange with λ_p and λ_n
B_ϕ	toroidal magnetic field
B_{rip}	toroidal field ripple
c_s	plasma sound speed
D	collisionless MHD interchange near $\beta_{critical}$
$D_\perp^{an}$	anomalous diffusivity
$\mathbf{e}_\parallel = \mathbf{b}, \mathbf{e}_\wedge, \mathbf{e}_\perp$	parallel, diamagnetic and radial unit vectors
e_σ	electric charge (–e for electrons, +Ze for ions)
$E_\perp^{SOL}$	radial electric field in the SOL

f_t	trapped fraction
f_{ELM}	ELM frequency (Hz)
F	drift wave
G1	MHD interchange
G2	endplate MHD interchange,
I_p	plasma current
J	drift with collisionless skin depth
K1	drift Alfven: low collisionality
K2	drift Alfven: high collisionality
L, L1	sheath and sheath-resistive modes
$L_{\|\|o}/L_{\|\|i}$	connection lengths from the outer mid-plane to the outer/inner target,
$L_{\|\|}$	generic connection length
$L_{\wedge}$	poloidal extent of the SOL
l_v	dissipative scale
$l_{\perp\sigma}$	radial dissipative scale
M	Mach number, $M = u_{\|\|}/c_s$
M^c_σ	critical Mach number
M	charge-exchange
n_σ	plasma (filament) density
$n_{e,u}$, n_e^{SOL}	upstream (SOL) plasma density
$n_{e,t}$	target plasma density
n_0	neutral density
n/n_{GW}	Greenwald fraction
$N_{\perp\sigma}$	average number of $\perp$ diffusive steps per $\|\|$ transport time
$N_{\perp}{}^{\chi}{}_{\sigma}$	average number of $\perp$ diffusive steps per $\|\|$ conductive time
N	Bohm scaling
O	collisionless skin depth
$p_\sigma = nT_\sigma$	static pressure
P_{heat}	heating power
P_{NBI}	Neutral Beam Injected power
P_{rad}	radiated power
P_{div}	power entering the divertor
$P_{rad,div}$	power radiated in the divertor
P_{ELM}	ELM power = $\Delta W_{ELM} f_{ELM}$
P_{SOL}	power entering the SOL
P_t	target deposited power
P_o/P_i	outer / inner target deposited powers
Q	null model, $\chi_\perp$ = constant,

$q_{\|\|}$	parallel energy flux
q_0 , q_{peak}	peak target heat load
q_o/q_i	outer/inner deposited peak heat loads
$q_{tot} \approx q_e + q_i$	total heat load = electron + ion heat loads
$q_{\sigma\wedge}^{E}$	as defined by (3.2)
$q_{\sigma\wedge}^{p}$	as defined by (3.2)
$q_{\sigma\wedge}^{T}$	as defined by (3.2)
$q_{\mu v,\sigma}$	μ component of the convective energy flux
$q_{\mu\chi,\sigma}$	μ component of the conductive energy flux
$q_{\mu\sigma}$	μ component of the total energy flux
$q_{\|\|\chi,\sigma}^{FS}$	free streaming (FS) parallel heat flux
q_{95}	safety factor at 95% poloidal flux surface
r_u	radial distance at the outer mid-plane
R	major radius
R_o/R_i	major radius of outer/inner mid-plane
ΔR_{out}, ΔR_{in}	outer/inner mid-plane wall gaps
$Re = \tau_v/\tau_u$	Reynolds number
s_t	distance along the target
S	magnetic shear
T_σ	plasma (filament) temperature
$T_{\sigma,u}$, T_σ^{SOL}	upstream SOL temperature
$T_{\sigma,t}$	target temperature
u	plasma (filament) velocity
u_v	characteristic velocity at the scale $\delta = l_v$
$v_{t\sigma}$	thermal speed, $v_{t\sigma} = (T_\sigma/m_\sigma)^{1/2}$
$v_{t\|\|\sigma}$, $v_{t\perp\sigma}$	parallel and perpendicular thermal speeds
$\mathbf{v}_E \sim \mathbf{E}\times\mathbf{b}/B$	electric drift velocity
ΔW_{ELM}	stored energy drop due to an ELM
X	direct ion orbit loss, λ_q^X
Y1	ion gyro-radius, ρ_i
Y2	poloidal ion gyro-radii, $\rho_{\theta i}$
Z1	electron gyro-radius, ρ_e
Z	atomic charge of main plasma ions

C.4 TERMINOLOGY

classical	$\chi_{\perp i} \propto q_{95}^{0}$
neo-classical	$\chi_{\perp i} \propto q_{95}^{2}$
(neo-)classical	$\chi_{\perp i} \propto q_{95}^{k}$ with $0 < k < 2$

near-SOL	SOL region with $r / \lambda_q < 2 – 3$
far-SOL	SOL region with $r / \lambda_q > 2 – 3$
fwd-B	forward toroidal field (**B**×∇B ↓) direction
rev-B	reversed toroidal field (**B**×∇B ↑) direction
LP, TC, IR	Langmuir probes, thermocouples, infra-red camera

REFERENCES

[1]. Y. Andrew et al., *Plasma Phys. Control. Fusion* **46** (2004) 337.

[2]. G.Y.Antar et al., *Phys. Plasmas* **8** (2001) 1612.

[3]. A.Bergmann, *Nuclear Fusion*, **42** (2002) 1162.

[4]. B.Beyer et al., *Plasma Phys. Control.. Fusion*, **41** (1999) A757.

[5]. D.Biskamp, Magnetohydrodynamic Turbulence, Cambridge U. Press, Cambridge, UK vv (2003).

[6]. J. Boedo et al., *J. Nucl. Mat.*, **337-339** (2005) 771.

[7]. X.Bonnin et al, *J. Nucl. Mat*., **313-316**, (2003) 909.

[8]. V.I.Braginski, in M.A.Leontovich (ed.), *Rev. of Plasma Physics*, Consultants Buraeau, New York, 1965.

[9]. A.V.Chankin, *J. Nucl. Mat.*, **241-243** (1997), 199.

[10]. A.V.Chankin et al., *J. Nucl. Mat*., **290-293**, (2001) 518

[11]. S.Chapman, T.G.Cowling, Mathematical Theory of Non-uniform Gases, Cambridge U. Press, UK (1958).

[12]. R.H. Cohen, T.D. Rognlien, *Contrib. Plasma Phys.* **34** (1994) 198.

[13]. J.W.Connor et al., *Nuclear Fusion*, **39** (1999), 169.

[14]. J.W. Connor and H.R. Wilson, *Plasma Phys. Control. Fusion*, **42** (2000), R1.

[15]. G. Councell et al., *J. Nucl. Mat.*, **266** (1999), 91.

[16]. G. Councell et al., *Plasma Phys. Control. Fusion*, **44** (2002), 827.

[17]. P. Diamond et al*., Plasma Phys. Control. Fusion,* **47** (2005) R35.

[18]. S.K.Erents et al., *Nuclear Fusion*, **40** (2000), 309.

[19]. T. Eich et al., *J. Nucl. Mat.*, **313** (2003) 919.

[20]. G.Federici et al., *Nuclear Fusion* **41** (2001) 1967.

[21]. U.Frisch, Turbulence, Cambridge U. Press, Cambridge, UK (1995).

[22]. W.Fundamenski et al., *J. Nucl. Mat.*, **290** (2001) 593.

[23]. W.Fundamenski et al., *Plasma Phys. Control. Fusion*, **44** (2002) 761.

[24]. W.Fundamenski et al., *J. Nucl. Mat.*, **313** (2003) 787.

[25]. W.Fundamenski et al., *Nuclear Fusion*, **44** (2004) 20.

[26]. W.Fundamenski et al., *Plasma Phys. Control. Fusion*, **46** (2004a) 233.

[27]. W.Fundamenski et al., *J. Nucl. Mat.*, **337-339** (2005) 305.

[28]. O.E.Garcia et al., *Phys.Rev.Lett.* **92**, 154003 (2004). Ph. Ghendrih et al*., Nucl. Fusion* **43** (2003) 1013.
[29]. J. Graves et al., *Plasma Phys. Control. Fusion*, **47** (2005) L1.
[30]. B.Goncalves et al., *Plasma Phys. Control. Fusion* **45** (2003) 1627.
[31]. R.D.Hazeltine, J.D. Meiss, Plasma Confinement, Addison-Wesley, Redwood, USA (1992).
[32]. P. Helander, D.J.Sigmar, Collisional transport in magnetized plasmas, Cambridge U. Press, Cambridge, UK (2002).
[33]. A. Herrmann et al., *J. Nucl. Mat.*, **313** (2003) 759.
[34]. J. D.Huba, NRL Plasma Formulary, *Naval Research Laboratory*, Washington, USA (2002).
[35]. A.Huber et al., *J. Nucl. Mat.*, **337-339** (2005) 241.
[36]. C.Hidalgo et al., *J. Nucl. Mat.*, **313-316** (2003) 863.
[37]. J.A.Heikkinen et al., *Phys. Plasmas*, **8** (2001), 2824.
[38]. J.Huggil, *Phys. Contr. Fusion* **42** (2000), R75.
[39]. I.H.Hutchinson et al., *Plasma Phys. Control. Fusion* **37** (1995) 1389. ITER Physics Basis, *Nuclear Fusion*, **39** (1999), 2137-2664,£4.2,£4.3.6.1,£4.4.
[40]. K.Itoh, S-I Itoh, A. Fukuyama, Transport and Structural Formation in Plasmas, IoP, Bristol, UK (1999).
[41]. J.W. Kim et al, *J. Nucl. Mat.*, **290** (2001) 644.
[42]. J.W. Kim, An Analysis of the Anomalous Transport of the Plasma Edge in ASDEX Upgrade, *Ph.D. Thesis*, U. Muenchen (2002).
[43]. G.Kirnev et al., *J. Nucl. Mat.*, **337-339** (2005) 271.
[44]. S.I.Krasheninnikov, *Physics Letters A,* **283** (2001) 368.
[45]. A.N.Kolmogorov, *Dokl.Akad.Nauk SSSR* **32**, 16-18 (1941), reprinted in *Proc.R.Soc.Lond.* **A 434**, 15-17 (1991).
[46]. B.B.Kadomtsev, Plasma Turbulence, Academic Press, New York, USA (1965).
[47]. A.Kallenbach et al., *Plasma Phys. Contr. Fusion* **46** (2004), 431.
[48]. A.Kukushkin et al, *Nuclear Fusion*, **42** (2002) 187.
[49]. B.LaBombard et al., *J. Nucl. Mat.*, **241-243** (1997) 149.
[50]. J.Lingertat et al., *J. Nucl. Mat.*, **241-243** (1997) 402.
[51]. G.F.Matthews et al., *Nuclear Fusion*, **43** (2003) 999.
[52]. G.F. Matthews et al., *J. Nucl. Mat.*, **290** (2001), 668.
[53]. K.Miyamoto, Plasma Physics for Nuclear Fusion, MIT Press, Boston, USA (1987).
[54]. Y.Nashimura et al, *Phys. Plasmas* **11** (2004) 115.
[55]. V.Naulin, et al. *New J. of Phys*. **4** (2002) 28.1.
[56]. V.Parail et al., *Plasma Phys. Control. Fusion* **44** (2002) A63.
[57]. C.S.Pitcher et al., *Plasma Phys. Control. Fusion* **39** (1997) 779.
[58]. R.A.Pitts et al., *J. Nucl. Mat.*, **337-339** (2005) 146.

[59]. T.W. Petrie et al., *Nuclear Fusion*, **43** (2003), 910.
[60]. V. Riccardo et al., *Plasma Phys. Contr. Fusion*, **43** (2001), 881.
[61]. T.D. Ronglien et al., *J. Nucl. Mat.*, **266-269** (1999), 654.
[62]. D. Rudakov et al., *J. Nucl. Mat.*, **337-339** (2005) 717.
[63]. B.Scott, Low frequency fluid drift turbulence in magnetised plasmas*, IPP report,* **5/92**, Max-Planck Gesselschaft, Garching, Germany (2001).
[64]. M.J. Schaffer et al., *Nuclear Fusion*, **37** (1997), 83.
[65]. K.C. Shaing et al., *Phys. Rev. Lett.* **63** (1989) 2369.
[66]. L. Spitzer, R. Harm, *Phys. Rev.* **89** (1953) 977.
[67]. P.C Stangeby, The Plasma Boundary of Magnetic Fusion Devices, IoP, Bristol, UK (2000).
[68]. B.Taylor, *Plasma Phys. Control. Fusion* **39** (1997) A1.
[69]. H.Tennekes, J.L.Lumley, A first course in Turbulence, MIT Press, Boston, USA (1972).
[70]. H.Thomsen et al., *Phys. Plasmas* **9** (2002) 1233.
[71]. X.Q.Xu, R. Cohen, *Contrib. Plasma Phys.* **38** (1998) 158.
[72]. X.Q.Xu et al , *J. Nucl. Mat*., **266-269**, (1999) 993.

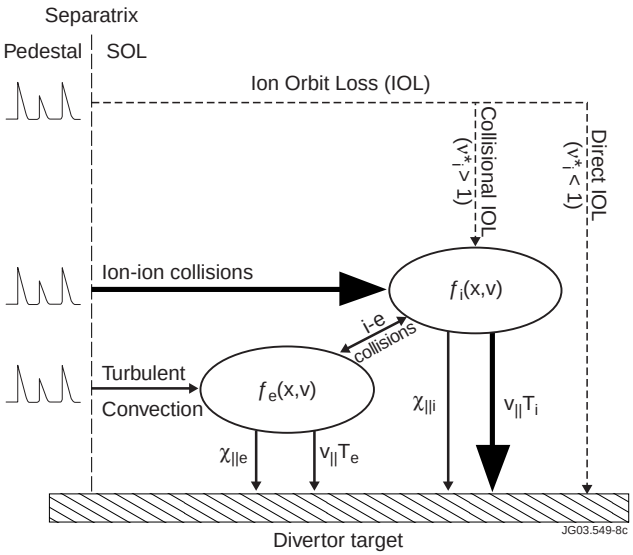

Figure 1: Schematic of power exhaust mechanisms in a diverted tokamak. The time series indicates that the indicated channels apply both to the inter-ELM phase and the ELM transients. This figure was adapted, with some modifications, from Fig.7 of [Fundamenski04].

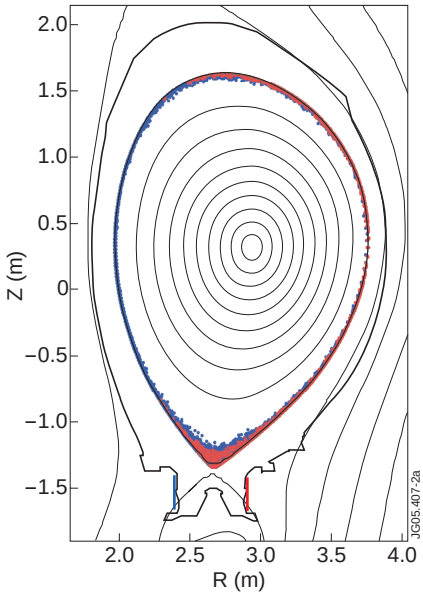

Figure 2(a): Results of ASCOT modelling of ion orbit loss in fwd-B. The initial launch location of ions has been labelled blue (black) if the orbit terminates at the inner target and red (grey) if it strikes the outer target.

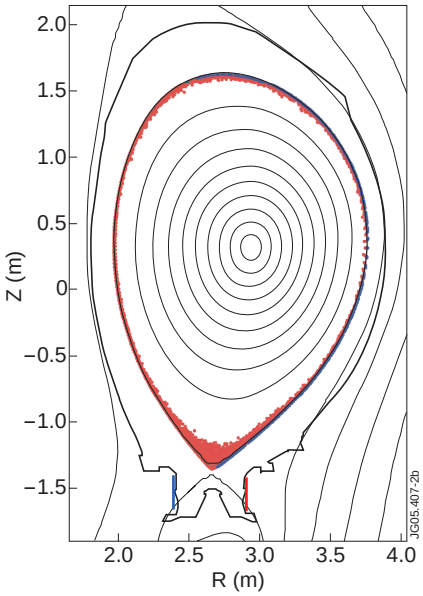

Figure 2(b): Same as Fig.2(b), but in rev-B.

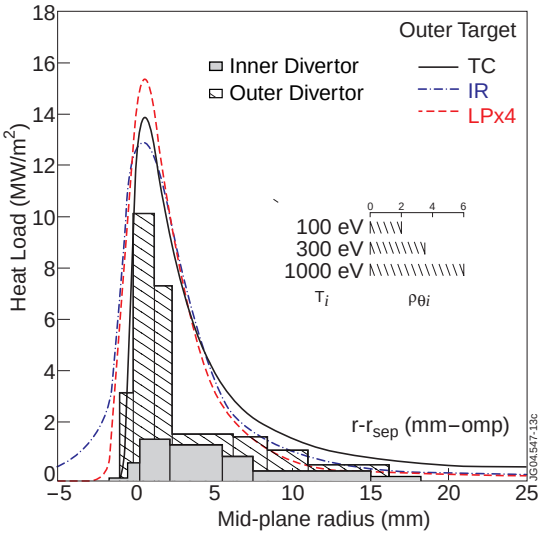

Figure 3: A comparison of TC (solid line), IR (dot-dash line) and LP (dashed line) measured steady-state power deposition profiles at the outer target for a 2.5MA/2.4T discharge for 16MW Type-I H-mode. The IR profiles have been averaged over the ELMs. The scale of the electron heat flux (LP) is four times smaller in the high power case. Also shown is are the profiles obtained for a 12MW Type-I H-mode (same field and current), using the shot-by-shot TC method. For comparison the poloidal gyro-radius at the outer mid-plane is shown for three values of the ion energy. The figure was adapted, with some modifications, from Fig.2(b) of [Fundamenski04].

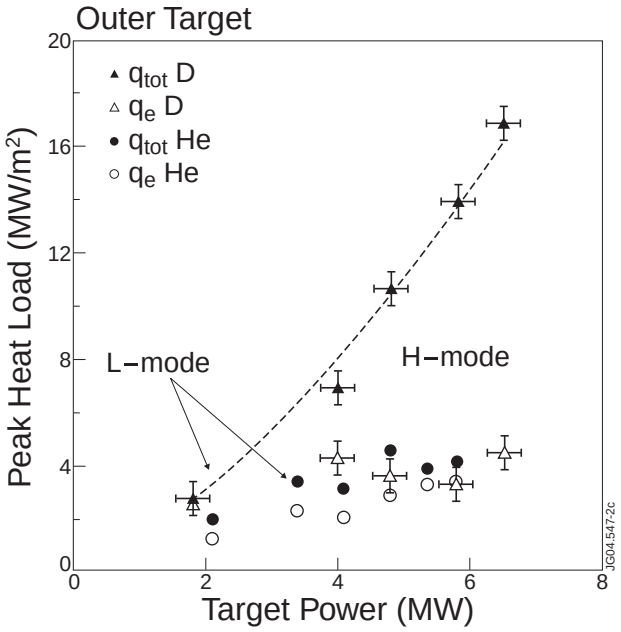

Figure 4: Steady-state total (TC) and electron (LP) peak heat loads for D and He plasmas as a function of power entering the SOL. The TC values increases faster than linearly with P_t. The excess power, which we identify with the ion contribution, $q_i = q_{tot} - q_e$, becomes more pronounced in D in high power H-modes. This figure was adapted from Figure 3 of [Fundamenski04].

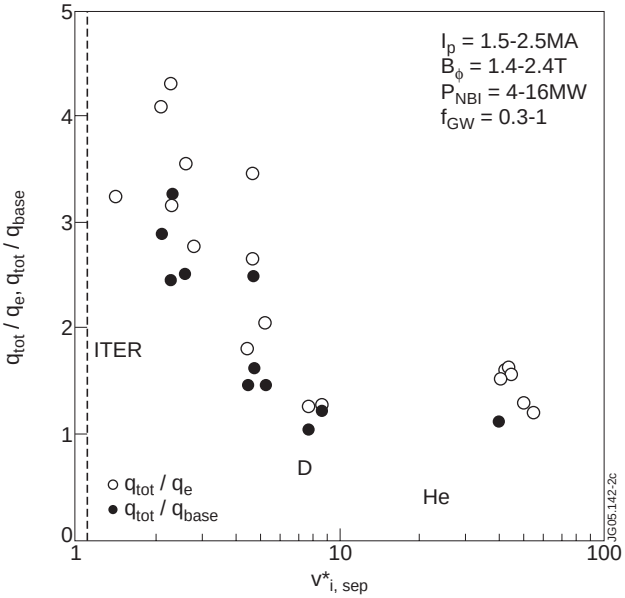

Figure 5: Ratio of total to electron peak heat loads, q_{tot} / q_e, and total to base heat loads, q_{tot} / q_{base}, as a function of the ion collisionality at the upstream separatrix. The anticipated ITER value is indicated by the vertical dashed line.

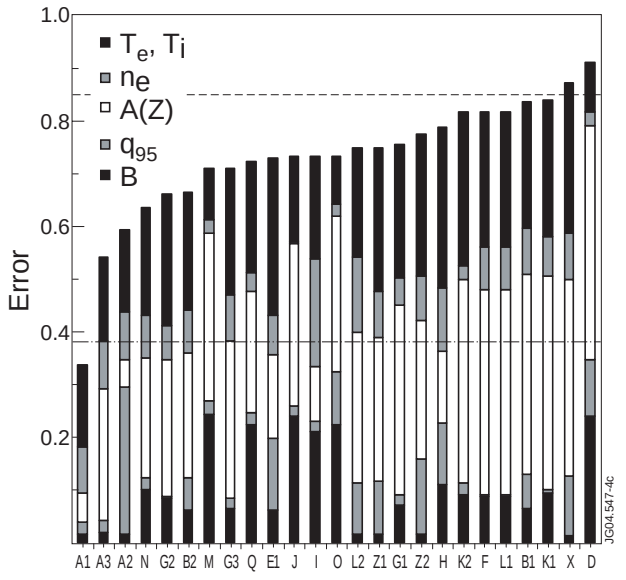

Figure 6: RMS error between theoretical and experimental λ_q exponents, assuming dominant || convection, showing contributions from (T_e, T_i), ne, Z(A), q_{95} and B_ϕ exponents. Dot-dashed line represents estimated measurement error, while the dashed line the average over all theories. The figure was adapted from Fig.6(c) of [Fundamenski04].

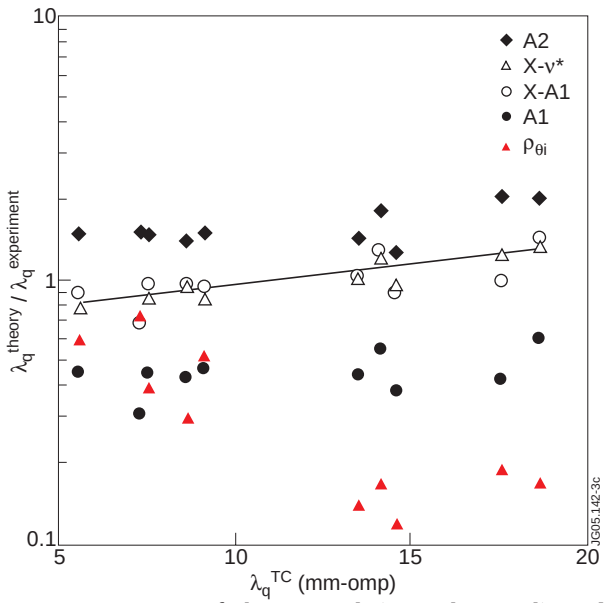

*Figure 7: Ratio of theoretical (neo-classical) and experimental λ_q values for: neo-classical and classical ion conduction, **A2** and **A1**, two collisional orbit loss estimates, **X**-n^* and **X-A1**, and the polodal gyro-radius, $\rho_{\theta i}$.*

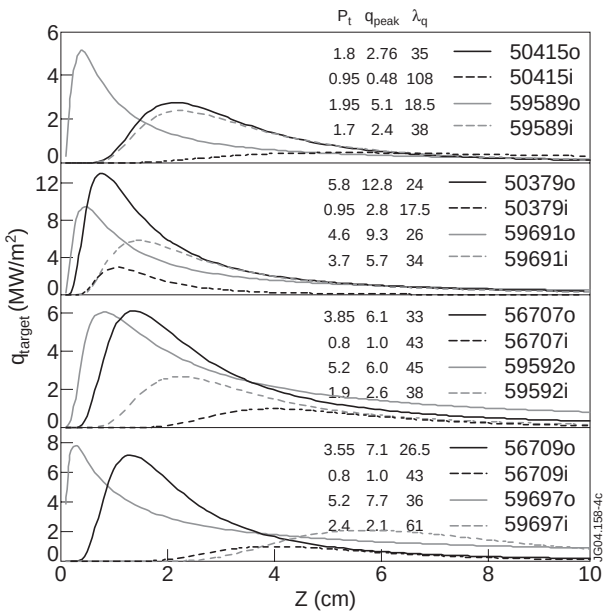

Figure 8: Target power deposition profiles obtained using the TC analysis for matched pairs of fwd-B and rev-B shots, see Table 1. The horizontal axis indicates vertical distance along the tile. Deposited powers, peak heat loads and integral power widths are tabulated.

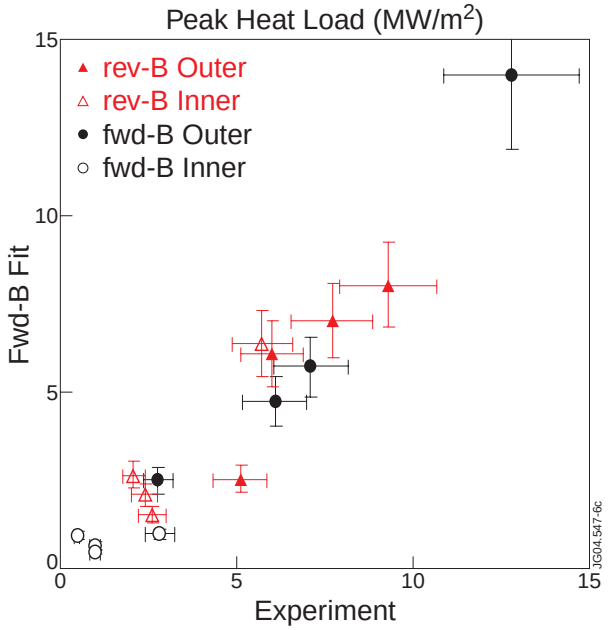

Figure 9: Comparison of outer target, total peak heat loads: best fit to all fwd-B data (2.1a) vs. the experiment, for both field directions and both targets. The figure was adapted from Fig.3 of [Fundamenski05].

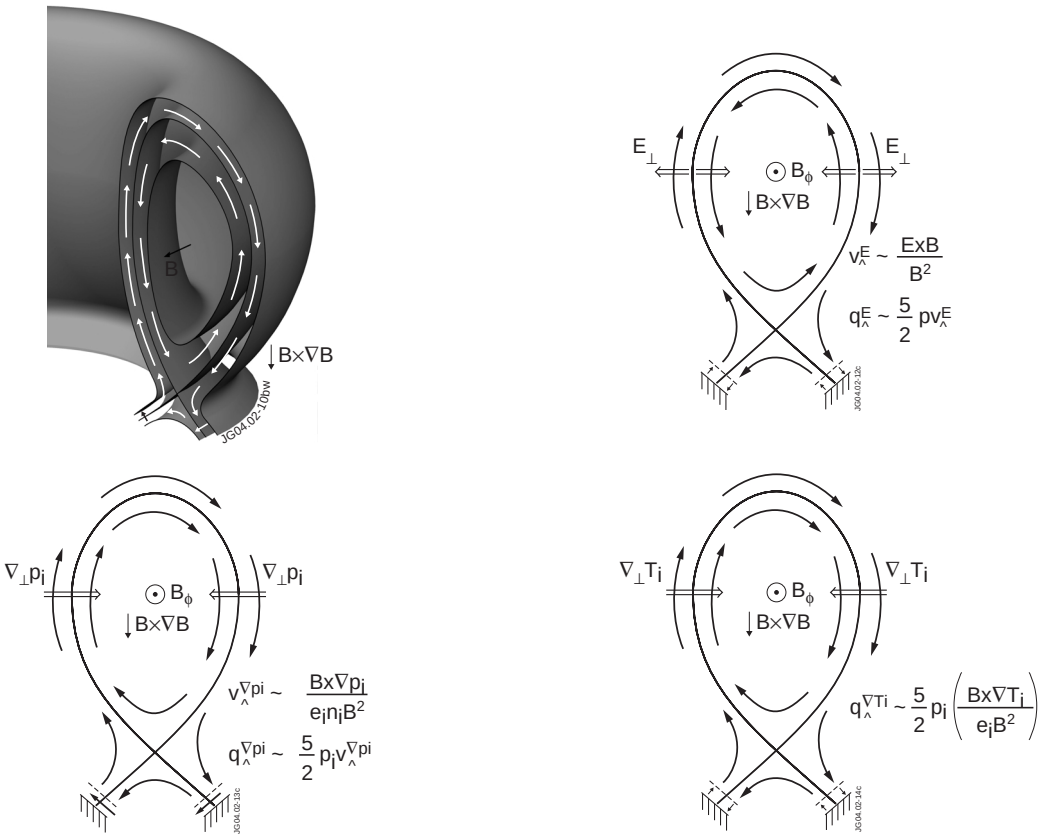

*Figure 10: Schematic of poloidal components of classical drift related energy fluxes (3.2) in the edge and SOL plasmas: convective **E×B** flux, diamagnetic ion convective and conductive fluxes.*

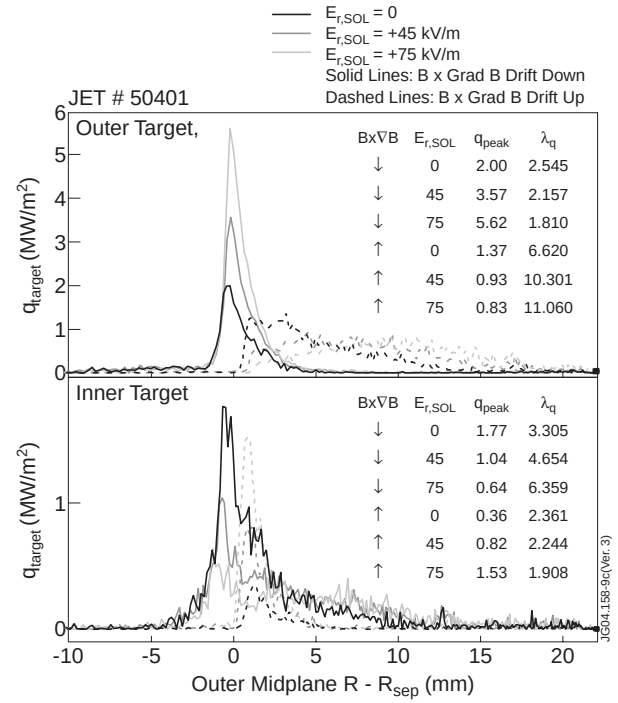

Figure 11: ASCOT modelling of (direct) ion orbit loss outer and inner target heat loads for 2.5MA/2.4T/12MA JET shot, with variation in field direction (fwd-B vs. rev-B) and $E_{r,SOL}$ (kV/m). The peak heat loads q_{peak} (MW/m^2) and power widths λ_q (mm-omp) are tabulated. The figure was adapted from Fig.5 of [Fundamenski05].

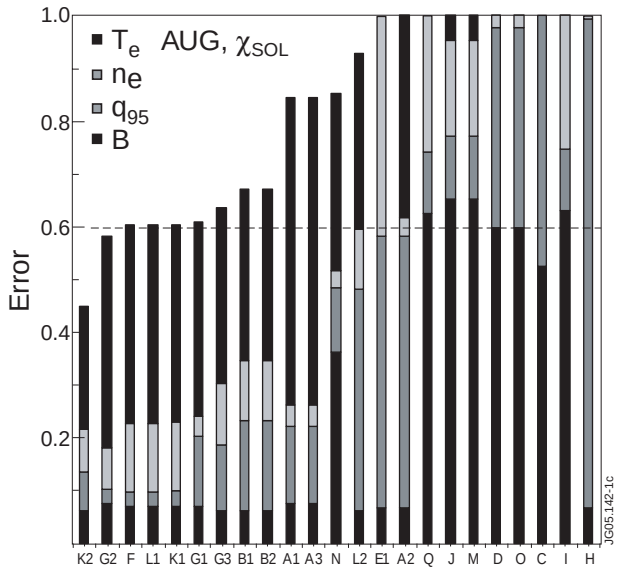

Figure 12: Similar to Fig.6, for the error between theoretical and experimental exponents of $c_\wedge$ scaling with T_e, ne, q_{95} and B_f obtained from SOLPS analysis of AUG plasmas, (4.1).

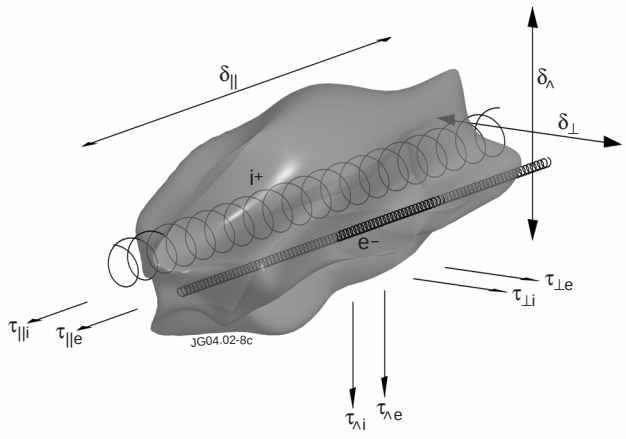

Figure 13: Plasma filament schematic: the size δ_μ and loss times τ_μ are indicated, where $\mu \in \{||, \wedge, \perp\}$ are the three magnetic directions. The envelope denotes a surface of constant electric potential. The gyration orbits of ions and electron are also indicated. The drawing is not to scale, since $\delta_{||} >> \delta_\wedge$, $\delta_\perp$ and $\rho_i >> \rho_e$. The filament need not be linear but follows the magnetic field lines, approximating a magnetic flux tube.

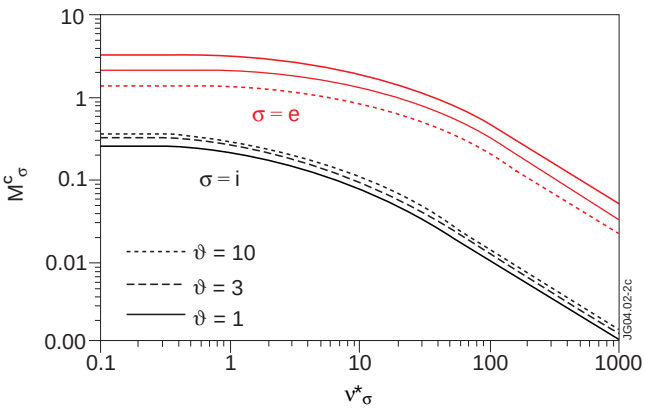

Figure 14: Critical Mach number $M^c{}_\sigma$ is given by (5.15) with $\tau_{\chi||\sigma}/\tau_{\nu||} \sim 1$, as a function of $\nu^*{}_\sigma$ for different values of $\vartheta = T_i/T_e$.

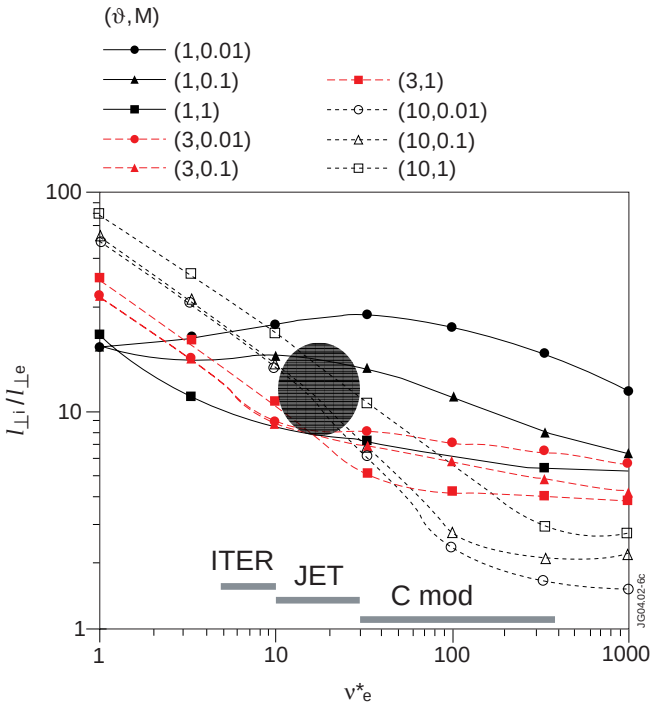

Figure 15: The ratio ion and electron thermal energy dissipative scales $l_{\perp i}/l_{\perp e}$ plotted vs. electron collisionality ν^*_e for different values of $\vartheta = T_i/T_e$ and Mach number M. The typical range of ν^*_e values for Alcator C-Mod, JET and ITER is indicated.

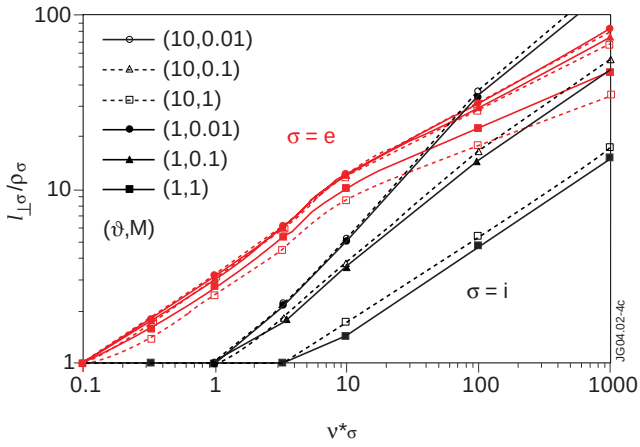

Figure A.1: Thermal energy dissipative scale normalized by the gyro-radius, $l_{\perp\sigma}/\rho_\sigma$ plotted vs. the collisionality ν^*_σ for both ions and electrons, for different values of $\vartheta = T_i/T_e$ and Mach number M.

Pulse	Bx∇B	Mode	I_p	B_ϕ	q_{95}	$<n_e>$	P_{heat}	P_{SOL}	j_s^{in}	j_s^{out}	T_e^{in}	T_e^{out}	T_e^{SOL}	n_e^{SOL}	f_{ELM}	ΔW_{ELM}	P_{ELM}	W_{ped}	$\Delta W/W_{ped}$
50415	↓	L	2.5	2.4	2.7	3.3	4.4	2.7	~2	3.9	~10	18	63	2.32	-	-	-	1.65	-
59589	↑	L	2.5	2.4	2.7	3.3	5.3	4.0	~4	~5	~25	~25	81	3.5	-	-	-	1.53	-
50397	↓	H-I	2.5	2.4	2.7	6.5	15.6	9.5	~2.5	4.0	~8	25	97	1.78	12	330	4	5.6	0.06
59691	↑	H-III	2.5	2.4	2.7	6.2	14.2	11.0	~6.5	~7	~25	~25	98	4.4	~30	~50	1.5	3.9	0.01
56707	↓	H-I	1.5	1.45	2.7	5.0	10.2	6.7	~1.8	2.2	~8	34	78	1.46	10	200	2	2.2	0.09
59592	↑	H-I	1.5	1.45	2.7	4.0	9.4	6.3	~2.5	~6	~20	~20	84	3.0	~40	~50	2	2.3	0.02
56709	↓	H-I	1.5	2.2	4.2	3.9	9.8	7.2	~1.5	1.8	~10	35	102	0.96	20	100	2	2.6	0.04
59697	↑	H-I	1.5	2.2	4.3	3.9	11.9	8.8	~5	~9	~20	~20	109	3.7	20	100	2	2.1	0.05

Table 1: Summary of matched pair discharges; all plasmas are D^+, NBI heated; units: I_p (MA), B (T), P (MW), n_e (10^{19} m^{-3}), T (eV), j_s (10^5 A/m^2), f_{ELM} (Hz), ∇W_{ELM} (kJ), W_{ped} (MJ); also used $L_{||}$ [m] ≅ 50×(q_{95}/2.6).

i-i	i-n	θ_0	ρ_0	$D_\perp^{an}$	$E_\perp^{SOL}$	Γ_o/Γ_i	q_o/q_i	P_o/P_i
0	0	0-2π	0.95-1	0	0	0.37, 5.62	0.27, 12.71	0.32, 15.32
1	0	0-2π	0.95-1	0	0	0.55, 7.18	0.30, 22.26	0.36, 26.73
1	1	0-2π	0.95-1	0	0	0.65, 6.81	0.34, 15.41	0.41, 18.58
1	1	0-2π	0.95-1	0	10	0.90, 4.21	0.39, 12.49	0.47, 15.02
1	1	0-2π	0.95-1	0	20	1.29, 2.63	0.50, 9.55	0.60, 11.53
1	1	0-2π	0.95-1	0	75	5.17, 0.56	1.09, 5.03	1.31, 6.08
1	1	0	1	0	0	9.06, 1.24	6.73, 1.46	8.15, 1.76
1	1	π	1	0	0	0.10, 20.34	0.12, 22.65	0.15, 27.23
1	1	0	0.95-1	0	0	2.22, 2.93	0.91, 7.47	1.10, 8.99
1	1	0	0.95-1	0	75	4.66, 0.81	0.94, 5.40	1.13, 6.50
1	1	0-2π	0.95-1	1	0	2.11, 1.66	1.55, 1.73	1.88, 2.09
1	1	0-2π	0.95-1	1	75	12.85, 0.26	3.83, 1.19	4.61, 1.42
1	1	0-2π	0.95-1	B_{rip}	0	0.67, 6.43	0.44, 15.72	0.53, 18.90
1	1	0-2π	0.95-1	B_{rip}	75	5.26, 0.57	2.22, 4.66	2.69, 5.63

Table 2: ASCOT trace run results: $n_i^{ped} = n_i^{sep} = 1.5e19$ m^{-3}; $T_i^{ped} = 1$ keV; $T_i^{sep} = 168$eV (omp); Maxwellian f(E,α) with local (n_i, T_i) For 2D (n_i, T_i) SOL plasma (JET 50401); Δ_{ped} = {0, 15} mm-omp; E_r^{core} = neo-classical. Results are listed for (fwd-B, rev-B).

$\mathbf{N_{\perp e}/N_{\perp i}}$	$\mathbf{M << M^c_e, \nu^*_e >> \nu^{*c}_e}$	$\mathbf{M << M^c_e, \nu^*_e << \nu^{*c}_e}$
$\mathbf{M << M^c_i, \nu^*_i >> \nu^{*c}_i}$	$1.21\times\vartheta^4$	$19.5\times\vartheta^4/\nu^*_e$
$\mathbf{M << M^c_i, \nu^*_i << \nu^{*c}_i}$	$0.31\times\vartheta^2\nu^*_e$	$5\times\vartheta^2$
$\mathbf{M >> M^c_i}$	$0.78\times M(1+Z/\vartheta)^{1/2}\vartheta^2\nu^*_e$	$12.5\times M(1+Z/\vartheta)^{1/2}\vartheta^2$

Table 3: Ratio of average number of electron and ion radial steps per || transport time, in the three asymptotic limits (B.2) - (B.4).